

Improving Strength of 3D Printed Parts through Stress-aligned Print Paths using highly anisotropic Liquid Crystal Polymers

Master Thesis
Nick Faber



Improving Strength of 3D Printed Parts through Stress-aligned Print Paths

using highly anisotropic Liquid Crystal
Polymers

by

Nick Faber

to obtain the degree of Master of Science
at the Delft University of Technology,
to be defended publicly on Friday November 26th, 2021 at 3:00 PM.

Student number:	4350979		
Project duration:	January 12, 2021 – November 26, 2021		
Thesis committee:	Dr. K. Masania	TU Delft	chair, daily supervisor
	Prof. C.A. Dransfeld	TU Delft	Examiner
	Dr. J. Wu	TU Delft	External examiner
	Dr. S. Gantenbein	NematX AG	External supervisor

An electronic version of this thesis is available at <http://repository.tudelft.nl/>.

Preface

This report is for my Master Thesis at the Aerospace Structures & Materials track of the Faculty of Aerospace Engineering at the TU Delft. It can be read as a stand-alone report. However, for additional information on the literature underlying this report, I would like to refer to my Literature review 'Nonplanar Fused Deposition Modeling'.

I would like to express my gratitude to Kunal and Silvan for their daily supervision. Their endless optimism and relaxed way of supervising, even during the harder times of this project, was a big driving factor that led to the successful result of this project. Another special thanks goes out to Caroline, who I consider a third supervisor by the amount of effort she has put into helping me. She speaks 3D printing and LCP fluently, and without it I would not have come this far. Next to that, I would like to thank Martin-Pierre Schmidt, who kindly provided the results from his research to me, and helped me with interpreting and using the data. For helping me out with all the issues I encountered when building the 5XM I would like to thank Yannick Nagel as well. Actually, I would like to thank the whole NematX team, for the fun and informative bi-weekly Friday afternoon meetings, and of course for providing the LCP filament for this project. Many thanks also go to the DASML staff, especially to Dave and Alexander, who never complained when I yet again changed all my plans regarding tests. And I could not have done it without all the help in the lab I got from my fellow SML members; Kevin, Berend, Lars, Ranjan, Satya and all the others. With whom I've spent a lot of time in The Lab, having a great time!

The project was a very challenging one, with it being very open in the beginning. It started with nothing more than 'Let's see if we can make a strong part using the anisotropic properties of LCP'. I am very happy with how it evolved into the project it has become. The hardest times were the ones stuck at home due to Covid, with nothing else to do than to write reports and debug codes. Luckily there was always the foresight of going back to the lab to tinker with 3D printers and try out cool stuff.

So with this thesis report, my time at the TU Delft will come to an end, and I am happy to enter my career as the well-educated engineer I have become. Ready to take on any challenges the future will bring me!

*Nick Faber
Delft, November 2021*

Abstract

Additive Manufacturing has made it possible to manufacture parts whose shape complexity was unfeasible with other traditional methods by depositing material layer-wise. However, this planar layer-wise deposition strategy can be restrictive for the part's properties. Indeed, lower strength is often encountered in the inter-layer direction due to weaker bonding between polymer beads. To solve this problem, many studies attempted to improve the adhesion between deposited polymer beads at the material scale. However, the anisotropic behaviour can also be embraced and used as an advantage. Therefore, in this thesis a different method is implemented: the Stress-Aligned Printing method, in which print-paths are oriented along the principal stress directions of a part's load case, thus breaking free from the traditional planar layer-wise deposition method.

To implement this stress-aligned printing method, the focus is set on the case study of a popology- and anisotropy- optimized bracket for a jet engine, extracted from Schmidt et al. (2020). Placing the print paths along the principal stress direction in a pure free-form fashion requires dedicated hardware. A 5-axis printer with high freedom of motion was developed, enabling highly curved non-planar print paths. Furthermore, the traditional algorithms (slicers), which split the part into print-paths in a planar fashion are not sufficient for this type of printing. Therefore a slicer for 5-axis printing was also developed that takes a set of stress lines as input and transforms them into printable lines. This includes filtering out invalid stress lines, sorting the print line order, determining the nozzle orientation, generating contour-following travel moves and applying the inverse kinematics of the 5-axis printer. The output of this algorithm is a G-code that can be used to print a stress-aligned object such as the jet engine bracket.

Liquid crystal polymer was chosen as the printing material due to its excellent mechanical properties along the print direction and thus, representing a highly anisotropic material. The material's microstructure consists of highly ordered nematic domains which align along the flow fields when extruded through a 3D printer nozzle. This alignment is retained after the material cools down thus creating a very strong bead of polymer. Single printed lines have been measured to withstand tensile stresses of up to 800 MPa and show stiffnesses of up to 35 GPa, while transverse tensile properties tend to be in the range of other thermoplastic printing materials (Gantenbein et al. (2018)).

The approach developed in this work was demonstrated for the jet engine bracket which was fabricated as two pieces. The bracket body and the two upper attachment points (lugs) were printed separately and joined for optimal transfer of the load to the stress-aligned body. A tensile test showed a failure point at 276.7 N due to a delamination in one of the fastening points. This failure happened at a non-stress-aligned area of the print, meaning that the stress-aligned part was not tested to its full potential. Nevertheless, while its mass has been reduced from 41 g to 20 g, this stress-aligned bracket experienced an increase of 156% on ultimate strength compared to the same bracket printed with the conventional planar method. While there are many challenges that still need to be resolved, this result gives a clear indication of the potential of the stress-aligned printing method

Contents

Abstract	v
1 Introduction	1
2 Related literature	3
2.1 Non-planar Fused Filament Fabrication review	3
2.1.1 Improving surface quality.	3
2.1.2 Printing supportless	4
2.1.3 Rapid volume printing	4
2.1.4 Improving structural properties.	5
2.2 Anisotropy	6
2.2.1 Continuous carbon fibre reinforced filament.	7
2.2.2 Liquid crystal polymers.	7
2.2.3 Topology- and anisotropy- optimisation	8
3 Thesis definition	11
3.1 Research gap and objective	11
3.2 Research questions	12
3.3 Scope: case study bracket.	12
3.4 Road map.	13
4 Experimental setup	15
4.1 Five-axis 3D printer.	15
4.1.1 Hardware	15
4.1.2 Control	18
4.2 Other printers	18
4.3 Mechanical tests	18
5 Results - Path generation	19
5.1 Support structure	20
5.2 Main body.	21
5.2.1 Generate stress lines.	21
5.2.2 Filter unusable print lines.	23
5.2.3 Turn-around sections.	23
5.2.4 Sort printing order	24
5.2.5 Travel moves	25
5.2.6 Print head orientation.	26
5.2.7 G-code generation	27
5.3 Upper lugs	28
5.3.1 Printing method.	28
5.3.2 Fastening method	29
6 Results - 3D Printing	31
6.1 LCP tensile specimens.	31
6.1.1 Test results	32
6.1.2 Conclusion	32
6.2 Bracket	33
6.2.1 Test results	36
7 Discussion	37
7.1 Bracket	37
7.2 Applicability of stress-aligned printing	38
7.3 Future research recommendations	39

A	Wiring diagrams 5-axis printer setup	43
B	Stream tracer parameters	47
C	LCP tensile specimens test results	49

List of Figures

1.1	Schematic representation of an FFF printer. Extracted from Turner et al. (2014)	1
2.1	CurviSlicer Algorithm. Progressively changes thickness of layers to reach optimal conformal outer surface. Left: Schematic visualisation of the algorithm. The top figure shows severe stair-step effect, while on the bottom figure it is almost eliminated. Right: Experimental result. Extracted from (Etienne et al. (2019)).	3
2.2	Supportless printing examples. A: Decomposition and separate slicing based on sharp edges between components. Extracted from (Ding et al. (2016)). B: Skeleton line extraction, continuous change of printing direction normal to skeleton line. Extracted from (Wang et al. (2019)). C: Examples of algorithm results for decomposing of non-trivial parts. Extracted from (2: Wu et al. (2020) 3: Xu et al. (2019) 4: Xiao and Joshi (2020)). D: Growing a print in a convex front. Extracted from (Dai et al. (2018)).	4
2.3	Wireprinting. Building the part from a mesh representation. A: Simple mesh on a 3DOF printer. Extracted from (Mueller et al. (2014)). B: Complex mesh on a robotic arm. Extracted from Huang et al. (2019)	5
2.4	Structural active-Z printing. Left: FEA stress trajectories and cross-section of resulting prints. Right: Three point bending test result. Extracted from Khurana et al. (2018)	5
2.5	Reinforced FFF. Topology optimized bracket printed in stress line direction using 5 axis FFF. A: Stress line vector field. B: Slicing result including supports. C: Printing setup. D: Results, comparison between planar and curved layers. Extracted from Fang et al. (2020)	6
2.6	Anisotropic properties of ABS. A: Ultimate tensile strength almost halved when tested transverse to printing direction. Extracted from Ahn et al. (2002). B: Similar results found in a study by Kubalak et al. (2019).	6
2.7	Continuous Carbon Fibre FFF. A: Schematic illustration of the working principle. B: Stress strain curve comparing PLA to Jute-fibre reinforced and Carbon-fibre reinforced specimens. Extracted from Matsuzaki, Ueda, et al. (2016)	7
2.8	3D printing of Liquid Crystal Polymers. A: Process of nematic domains self aligning while extruding. B: Microscopic image of broken LCP fibre showing clear shell-core like structure. C: Strength of a single line of 3D printed LCP with respect to layer height. Extracted from Gantenbein et al. (2018)	8
2.9	Topology optimization algorithm including optimal fibre orientation. A: 2D cantilever beam without filtering for smooth fibre orientation variation. B: Cantilever beam with smoothly changing fibre orientations. C: 3D case, a topology optimized bracket. D: Fibre direction within the bracket, which are smoothly varying.	9
3.1	The case study part for this research. A topology optimized bracket by Schmidt et al. (2020)	13
3.2	Load cases of the Grabcad & GE bracket optimization challenge. For this project load case 3 was chosen. Extracted from GrabCAD (2013).	13
3.3	Road map for research project divided into 3 major phases.	14
4.1	The 5AXISMAKER in the Shaping Matter Lab. 5-Axis FFF printer used for this research.	16
4.2	Extra printing clearance given by attaching the long nozzle. The insulation to maintain higher temperatures can also be seen.	16
4.3	Modifications to the 5XM. A: Before modifications. B: Custom z-axis extension to attach the slip ring. C: Slip ring and new Hemera extruder fitted.	17
4.4	Curved tube printed by the 5-axis printer as a full integration test of the machine.	17
4.5	Test setup with an example PLA bracket installed.	18
5.1	Division strategy for printing the SA Bracket.	20

5.2	Test print of LCP on PLA. Small warpage of the PLA is visible. Releasing the LCP square was no problem	20
5.3	Finished PLA support structure/mould to print the bracket on.	21
5.4	Complete workflow for generating the full print path of the SA bracket. 1: Stress lines are generated from vector field in Paraview, 2: Invalid lines are filtered out, 3: The attachment points are added connecting all the stress lines on one side, 4: The print lines are ordered such that they will print bottom up, 5: Travel moves are added making it one continuous print path, 6: Normal direction for the print head is determined, 7: Inverse kinematics determines 5XM axis position which is written into a G-code file.	22
5.5	A: Visualisation of the vector field generated by the algorithm in Schmidt et al. (2020). Coloured according to curve radius. B: Resulting stress lines after RK4 integration of the vector field by ParaView	23
5.6	Six stress lines connected by a turn-around section into three continuous lines	24
5.7	The stress lines colour-coded into their respective attachment point group.	24
5.8	Lower (Blue) and Higher (Green) travel move options.	26
5.9	Guide surface for the SA bracket. Nozzle will always stay normal to this surface, which will ensure smooth axis movement.	27
5.10	Schematic overview of 5XMonkey script	28
5.11	B and C axes offset definition	29
5.12	Schematic illustration of the print paths in the upper lugs. The paths run concentric around the hole, and along the pins. The bottom part does not show clear lines since it will be thermoformed, and thereby lose its anisotropic behaviour.	30
6.1	LCP tensile specimens printed under different orientations. A: Flat on heated bed. B: Vertically against a wall. C: Diagonally against an incline.	31
6.2	Stress strain diagram of a selection of LCP tensile specimens, showing the differences in properties	32
6.3	LCP tensile test progression. A: Pristine sample. B: First lines started to fail, minor dip in measured force. C: Second failure, the front layer has severed, large dip in measured force. D: Full failure of the specimen determining the ultimate strength.	33
6.4	Printing process of the main body on the 5XM. A couple of snapshots throughout the print are taken.	34
6.5	Printing and fastening process of the upper lugs. A: Upper lugs as they came out of the printer. B: Pins inserted through nine holes that were made with a soldering iron. C: Pin heads flattened out and integrated with the bracket.	35
6.6	Test specimens. A: SA Bracket, B: Planar Bracket	35
6.7	Tensile test results of the SA bracket and the planar printed bracket. Pictures of failures included.	36
7.1	Topology optimisation with varying ratio of anisotropy. It is clear that it would be beneficial to have junctions isotropic (red) while the legs should be anisotropic (green). Extracted from Schmidt et al. (2020)	38
7.2	Resulting intertwined junction at the attachment point. The randomness in the printing order of the lines makes this junction highly intertwined.	39
7.3	2D representation of how variable extrusion rate and adding tween lines can increase the density of a print.	40
7.4	Possible improved travel move, smoothly transitioning between the lower and higher options.	41
A.1	Wiring table of the slipring	44
A.2	Pinouts of the connectors before and after the slip ring	45
A.3	Internal wiring diagram of heated bed control box. Which both supports temperature control of a 360 V AC and 24V DC heating device.	46
B.1	Parameters used for the stream tracer in ParaView	48
C.1	Tensile tests of all the LCP test specimen	50

List of Tables

5.1	Example G-code with explanation of the lines	19
6.1	LCP tensile specimens overview.	32
C.1	Overview of all tensile specimen	49

Nomenclature

Abbreviations

5XM	5AXISMAKER
ABS	Acrylonitrile Butadiene Styrene
AM	Additive Manufacturing
CAD	Computer Aided Design
CAM	Computer Aided Manufacturing
CNC	Computer Numerical Control
CRFP	Carbon Fibre Reinforced Plastic
DOF	Degrees of Freedom
FEA	Finite Element Analysis
FFF	Fused Filament Fabrication
GE	General Electric
LCP	Liquid Crystal Polymer
PID	Proportional Integral Derivative
PLA	Polylactic Acid
PSU	Power Supply Unit
RK4	4th order Runge-Kutta integration method
SA	Stress-Aligned
SML	Shaping Matter Lab
TAO	Topology- and Anisotropy- Optimisation
TO	Topology Optimisation

Introduction

In 2009 the patent by Scott Crump of Stratasys expired. This patent was called 'Apparatus and Method for creating Three-dimensional Objects' (U.S. Patent No. 5,121,329, 1992), which was the invention of what nowadays is called 3D printing by the Fused Filament Fabrication (FFF) method. Since the expiry, multiple companies started to make FFF machines, and the rapid growth of the 3D printing market started. This market was very much aimed at rapid prototyping of parts but is now slowly shifting towards manufacturing of end-use parts, even for structurally demanding applications.

FFF is only one of the many 3D printing techniques such as Stereolithography, Selective Laser Sintering, and Direct Ink Printing (Gibson et al. (2010)). However, this project will only be using the FFF technique as it give the best material properties of the polymeric AM techniques. This technique consists in a thermoplastic polymer being heated and extruded through a small nozzle. The force is provided by the extruder, which pushes down on the filament (a roll of polymer). The nozzle lays down a bead of plastic on a surface (called the build-plate), and linear actuators move the nozzle to create a surface with the desired shape. When this surface is completed, the nozzle moves up a little (or the build-plate moves down) and the printer starts depositing a new layer of polymer on top of the previous one. This is repeated until the stack of layers forms the final geometry. A schematic FFF printer layout can be seen in Figure 1.1.

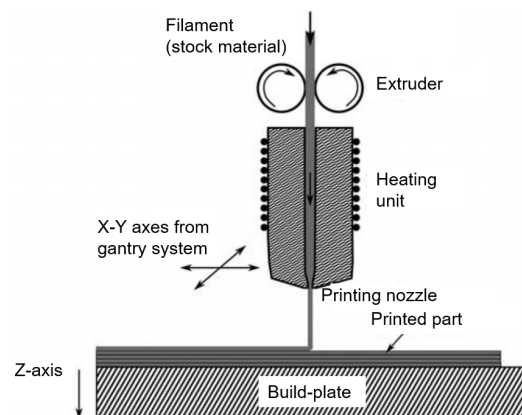


Figure 1.1: Schematic representation of an FFF printer. Extracted from Turner et al. (2014)

A crucial step for this technique is the print path planning, called 'slicing', which has to be conducted before every print. A so-called 'slicer' is a piece of software able to slice the part up into layers and then decide on the toolpath to take by the nozzle. This trajectory is called the print path. The slicer is also able to translate this toolpath into machine coordinates, and write it down in machine language, thereby generating the G-code. Well known slicers are Cura (Ultimaker (2020)), and the open-source Slic3r (Rannelucci, A. (2011)). The slicer includes the option to print the part with support structures. Since the printer deposits layers from bottom to top, any overhanging structure will be printed in mid-air, which is impossible. The nozzle needs to extrude the polymer on top of an already existing structure or else it will collapse and lose its geometry, leading to a failed print. Therefore, overhanging features of greater than 45° are usually printed with a supporting structure under them. This is purely done to make the printing possible, and the support is to be removed after the print is done. Infill structures are used to speed up printing time. The outer wall is printed parallel to the surface, but the core of the part is sparsely populated with polymer, leaving large air gaps. Thus the geometric shape of 3D model can be recreated with minimal material and time usage.

The transformation of 3D printing from a prototyping solution towards a manufacturing technique for end-use parts has led to improvements on this simple slicing approach as well as on the materials and processes used. To this end a lot of research has been focused on making 3D printed parts as isotropic as possible by utilizing heated print environments and improving the print line adhesion of materials. However, an alternative approach is to accept the anisotropic behaviour of FFF printed materials and optimize the slicing algorithm to accommodate for this anisotropy. The potential of this approach has been further improved by developments in 3D printing materials with even higher levels of anisotropy such as continuously fibre-reinforced polymers as well as liquid crystal polymers (LCP).

This project uses these recent developments in the research field of FFF aiming to create structurally improved parts and thus aiding the transition of FFF towards more structurally demanding applications. In Chapter 2 the related work from existing literature is presented, starting with an overview of non-planar FFF research, and ending with an explanation of two papers that form the basis of this research. In Chapter 3 the outline of the thesis project is presented followed by Chapter 4 where the experimental setup is given. The results of this study are highlighted in the following two chapters. The first one, Chapter 5, explains the algorithm developed for creating stress-aligned print paths. The second one, Chapter 6, presents the resulting prints from this algorithm and the final improvement in strength. The report is concluded with a discussion of the results and recommendations for future research in Chapter 7.

2

Related literature

For this thesis, an extended literature review into the state-of-the-art of non-planar FFF was performed and is summarized in the first section of this chapter. The second section will be assigned to elaborating the two most relevant papers for this thesis.

2.1. Non-planar Fused Filament Fabrication review

Non-planar FFF printing covers a broad range of approaches from simply using the z-axis on a 3 degrees-of-freedom (DOF) printer within one layer to get slightly curved layers, to full 12 DOF dual robotic arm setups to obtain full shaping freedom. In this review, four different reasons for using non-planar FFF were identified:

1. Improving surface quality.
2. Printing supportless.
3. Rapid volume printing.
4. Improving structural properties.

For each of these categories, an overview will be given in the following four subsections. More details can be found in the literature review report (Faber (2020)).

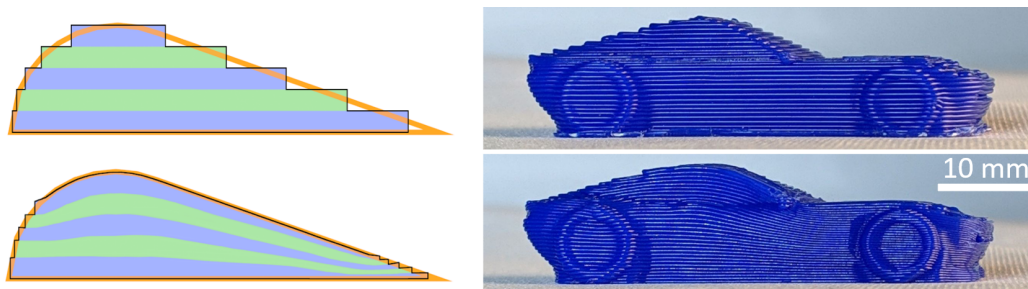


Figure 2.1: CurviSlicer Algorithm. Progressively changes thickness of layers to reach optimal conformal outer surface. Left: Schematic visualisation of the algorithm. The top figure shows severe stair-step effect, while on the bottom figure it is almost eliminated. Right: Experimental result. Extracted from (Etienne et al. (2019)).

2.1.1. Improving surface quality

The improvement of surface quality mainly aims to overcome the 'stair-step effect' problem. This happens when there is a discrepancy between the desired shape and the representation of the shape in slices, as can be seen in Figure 2.1. While achieving surface quality is not the main aim of this project, inspiration from the solutions to this problem can be taken. In fact, while improving the surface quality by printing curved layers, one may simultaneously improve the structural performance of a part, by

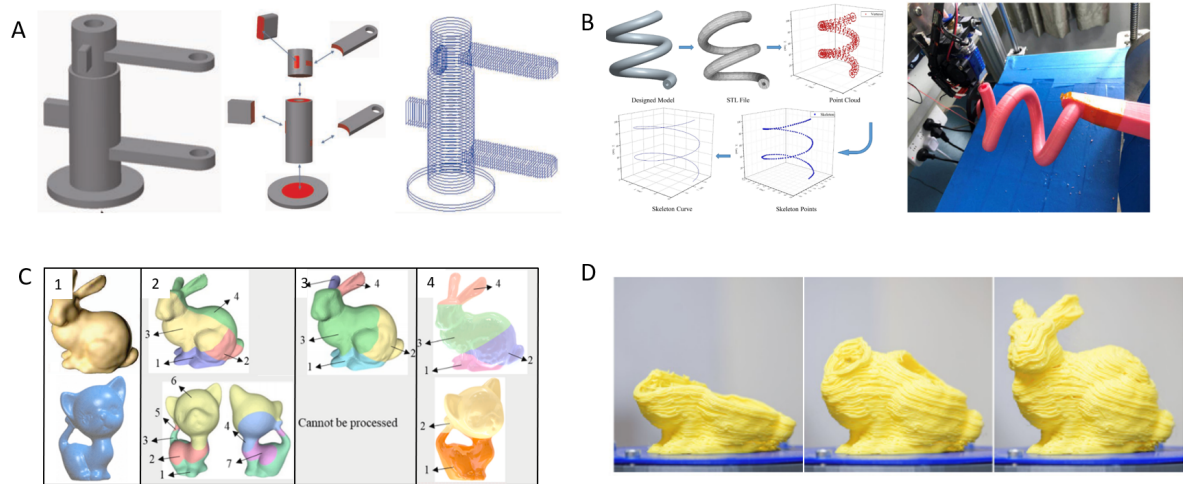


Figure 2.2: Supportless printing examples. A: Decomposition and separate slicing based on sharp edges between components. Extracted from (Ding et al. (2016)). B: Skeleton line extraction, continuous change of printing direction normal to skeleton line. Extracted from (Wang et al. (2019)). C: Examples of algorithm results for decomposing of non-trivial parts. Extracted from (2: Wu et al. (2020) 3: Xu et al. (2019) 4: Xiao and Joshi (2020)). D: Growing a print in a convex front. Extracted from (Dai et al. (2018)).

reducing the amount of 'free edges' in the layered print. A recent example of improving the surface quality by non-planar FFF is the research by Etienne et al. (2019). They developed 'Curvislicer', a slicing algorithm that progressively changes the layer thickness to reach a surface conformal outer skin. It is illustrated in Figure 2.1.

2.1.2. Printing supportless

FFF printing always requires an underlying surface to be printed on. One cannot just simply start printing in mid-air, since this will lead to the collapse of the part. For parts with large overhanging features, this poses a problem. In planar 3-axis printing, printing supports is the solution to this issue. However, printing time, material usage and required manual labour are increased, while the printing quality is decreased. In short, the non-planar strategies for printing supportless are:

1. Decomposition of features in a part, slicing them separately and assembling the toolpaths. This works best for parts where the decomposition is more obvious, with sharp edges between components.
2. Finding a skeleton line and slicing normal to that line. This is thus a continuous change of print orientation. This works best for long extrusion-like profiles.
3. Deciding on discrete cutting planes and changing the part orientation several times during a print. Different algorithms are written to find the optimum cutting planes minimizing the number of cuts needed. This is aimed at parts where the decomposition is less obvious, without sharp edges between components.
4. Growing the print in a convex front, resembling a growing half-sphere. This also works best for parts without sharp edges between components.

A graphical representation of these techniques is shown in in Figure 2.2.

2.1.3. Rapid volume printing

3D printing can sometimes take multiple days (Gibson et al. (2010)). In light of the search for faster prototyping, researchers have proposed wireframe printing. Here, a mesh representation of the part is printed. It is possible on a 3-axis printer, like in Mueller et al. (2014), but more complicated meshes required machines with 5 axes or more, like in Huang et al. (2019). The results can be seen in Figure 2.3.

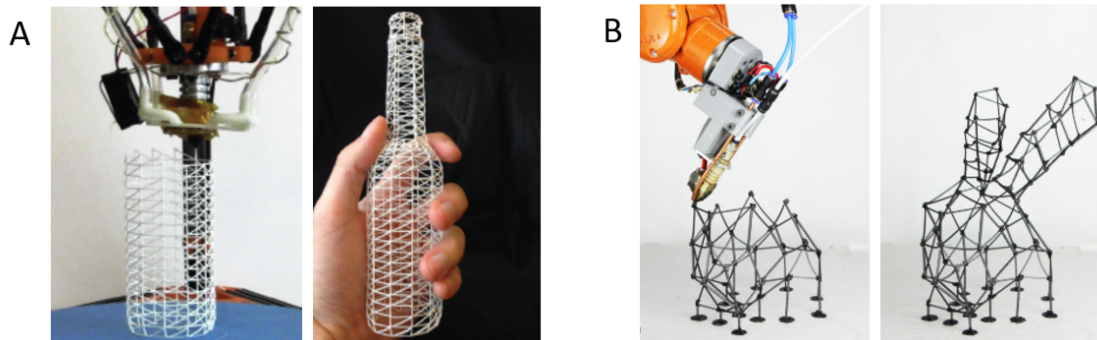


Figure 2.3: Wireprinting. Building the part from a mesh representation. A: Simple mesh on a 3DOF printer. Extracted from (Mueller et al. (2014)). B: Complex mesh on a robotic arm. Extracted from Huang et al. (2019)

2.1.4. Improving structural properties

The main objective of this research is to increase the structural performance of FFF printed parts. Using non-planar FFF much more shaping freedom is gained, thus printing along the stress direction becomes feasible. A simple example that illustrates the potential of this idea is by Singamneni et al. (2012). The authors have printed a simple bridge-like structure and compared planar slicing with slightly curved layers along the stress direction. They find an improvement of 40% in ultimate strength while weight and printing time remained equal. Yerazunis et al. (2016) printed a small dome structure on a 5-axis machine, which was tested by putting it under an air pressure difference. They printed along the hoop stress direction and found an improvement of 150%, from 0.97 MPa to 3.38 MPa in ultimate pressure.

More complicated load cases are analyzed in Khurana et al. (2018). A Finite-Element Analysis (FEA) is performed on a simply supported beam to extract the stress lines. Then the z-axis on a 3DOF printer is used to change the thickness in layers, such that the final cross-section follows these stress lines. It can be seen in Figure 2.4 that a 12.75% increase in ultimate strength is achieved.

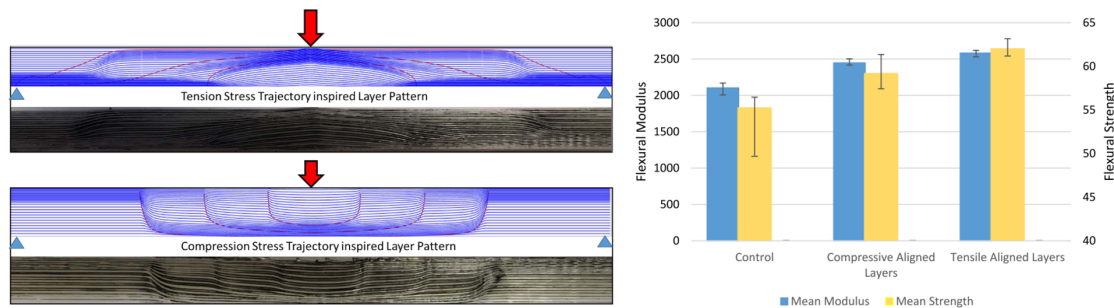


Figure 2.4: Structural active-Z printing. Left: FEA stress trajectories and cross-section of resulting prints. Right: Three point bending test result. Extracted from Khurana et al. (2018)

The next step in improving the structural properties is found in the 'Reinforced FFF' method by Fang et al. (2020). The authors have developed an algorithm that uses FEA results of any part to generate layers that lie along the stress lines. This result requires at least 5 DOF to be printed since the layers are highly curved. They reach an improvement of 102% on the ultimate strength of a topology optimized bracket. A visual representation of the algorithm can be seen in Figure 2.5.

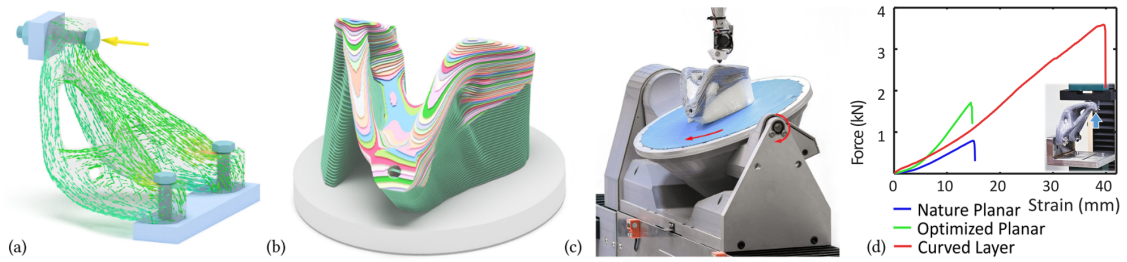


Figure 2.5: Reinforced FFF. Topology optimized bracket printed in stress line direction using 5 axis FFF. A: Stress line vector field. B: Slicing result including supports. C: Printing setup. D: Results, comparison between planar and curved layers. Extracted from Fang et al. (2020)

2.2. Anisotropy

This thesis project is based on one major physical property of FFF parts, their anisotropic mechanical behaviour. To explain it one must understand how bonds between adjacent beads are formed. Turner et al. (2014) states that the severeness of the anisotropy strongly depends on the thermal history of that bead. If the time elapsed between deposition of two beads is sufficiently short (less than 2 seconds), the first bead is still above its melting temperature and the two beads will fuse as one. If this time is longer, the temperature on the interface does not reach melting temperature but does reach above the glass transition temperature, and molecular diffusion prevails, which creates a weaker bond. The higher the initial temperature of the already deposited bead, the longer this temperature stays above the glass transition temperature, the stronger the bond will be. One can imagine that between two different layers the time is even longer than between two different beads, so the bonding will be even weaker. Therefore, FFF parts are usually strong in the printing direction, a lot weaker transverse to that, and weakest between layers. This rule stays consistent in many works, as can be seen in Figure 2.6 as an example. It must also be noted that this anisotropic behaviour is usually much less visible when considering stiffness, since both axially and transversely it is still the same material.

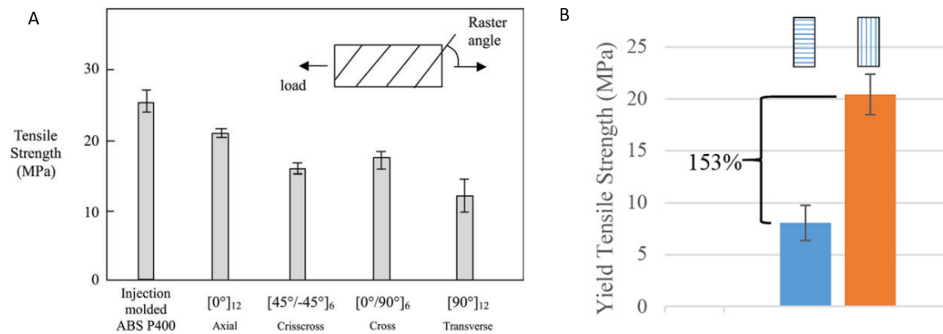


Figure 2.6: Anisotropic properties of ABS. A: Ultimate tensile strength almost halved when tested transverse to printing direction. Extracted from Ahn et al. (2002). B: Similar results found in a study by Kubalak et al. (2019).

2.2.1. Continuous carbon fibre reinforced filament

In an effort to make stronger FFF parts Matsuzaki, Ueda, et al. (2016) investigated extruding continuous bundles of carbon fibre together with a thermoplastic resin, using a 3 DOF machine to steer the fibres. These Carbon fibre reinforced plastic (CFRP) filaments are much stronger and stiffer, which can be seen in Figure 2.7. The ultimate strength of a single deposited bead was measured as high as 254MPa. This makes it very promising to use in combination with stress-aligned printing. However, there are some downsides to using this filament. One is that it requires a complete redesign of the printer, thus a special FFF printer has to be purchased to work with the material. It is also much less environmentally friendly since the carbon fibres themselves are not recyclable and energy-intensive to produce. But the largest downside is that the bending radius of CFRP filaments is limited. Since the carbon fibres bundles are very stiff, tight corners are problematic and require interruption of the continuity of the bundle, which is detrimental to the strength of the part. In a study by Matsuzaki, Nakamura, et al. (2018) it was found that radii smaller than 4 mm were not achievable.

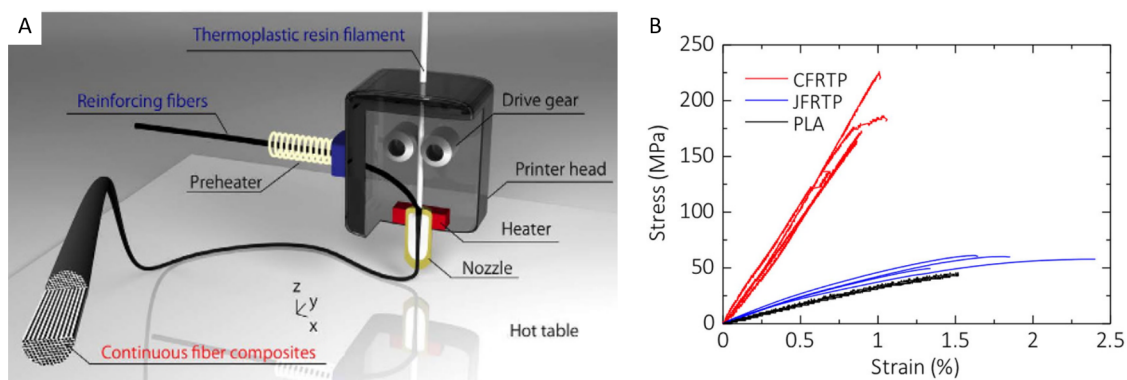


Figure 2.7: Continuous Carbon Fibre FFF. A: Schematic illustration of the working principle. B: Stress strain curve comparing PLA to Jute-fibre reinforced and Carbon-fibre reinforced specimens. Extracted from Matsuzaki, Ueda, et al. (2016)

2.2.2. Liquid crystal polymers

In recent research by Gantenbein et al. (2018), another material was found which exhibits these anisotropic material properties to an extreme. This material, Liquid Crystal Polymer (LCP), has nematic domains in its microstructure where the polymer chains are locally aligned. These domains are all oriented differently macroscopically, creating an isotropic material in its molten form at rest. However, during the process of extrusion through the printing nozzle, these domains align due to shear and elongational forces in the flow. After deposition, when the polymer bead cools down, these aligned domains are 'frozen' starting from the outer surface. The core of the bead does not cool as quickly and the material returns to its isotropic state. In essence, it turns into a composite material by itself, with a strong outer shell and a softer and ductile core, which is visible in Figure 2.8. With reducing bead height, the shell-to-core ratio increases, and thus the mechanical properties increase. A single 3D printed LCP line is measured to withstand 600 MPa for a layer height of 0.1 mm, and 800 MPa for 0.05 mm. The fibrous nature of the material also means it performs similar to a fibre-reinforced composite material while only containing a single polymeric phase. In an open-hole tensile test, isotropic (injection moulded) LCP failed at 20 MPa, while a 3D printed LCP panel failed at 100 MPa. When directing the printing lines around the hole, the panel failed at 200 MPa, illustrating the huge potential of using this material for stress-aligned FFF.

This material has thus shown to exhibit similar properties as CFRP filaments, with one advantage. Indeed, since the whole material melts in the nozzle it is not stiff at all, it only becomes stiff after it has been deposited. This means the steering radius of LCP is not limited, as is the case with continuous carbon fibre reinforced filaments. Therefore, the material is much easier to work with and provides more shaping freedom. Moreover, it can be used in any ordinary FFF printer that is able to reach 300°C, meaning little to no modifications to a printer have to be made to use the material. Additionally, aligning the nematic domains is a fully reversible process which means that LCP is recyclable, unlike CFRP filaments.

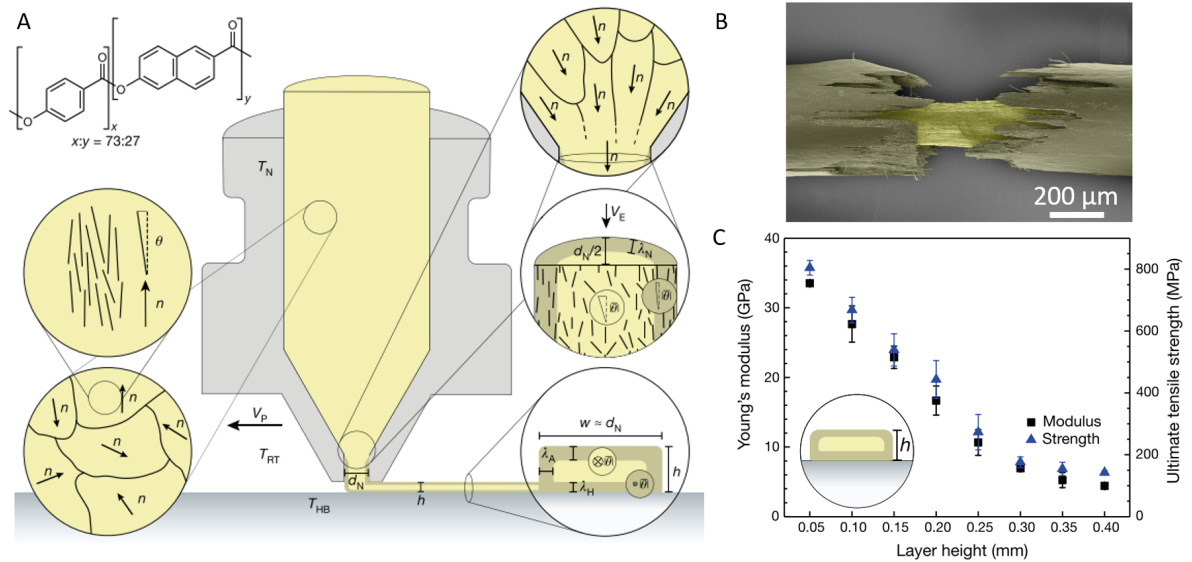


Figure 2.8: 3D printing of Liquid Crystal Polymers. A: Process of nematic domains self aligning while extruding. B: Microscopic image of broken LCP fibre showing clear shell-core like structure. C: Strength of a single line of 3D printed LCP with respect to layer height. Extracted from Gantenbein et al. (2018)

2.2.3. Topology- and anisotropy- optimisation

The potential of using these anisotropic materials leads to the question of how to deposit these materials optimally. The research by Schmidt et al. (2020) is aimed at answering that question. The authors present an algorithm that performs a density-based topology optimisation on parts, which by itself is not new. However, in this algorithm the local material orientation is also an optimisation variable. This means both the material density and its orientation are synchronously optimized. On top of that, the material orientation is enforced to change smoothly as to prevent small radii of bending. Another feature is that the optimisation can be run for multiple load-cases at once.

This algorithm works for both 2D and 3D designs. In the 2D case, this makes it applicable to for instance the Automated Tape Laying (ATL) and Direct Fibre Placement (DFP) manufacturing methods. It could also be used for planar 3D printing. However, for parts with load paths running out-of-plane the 3D method is more interesting. This algorithm is currently only bound to the computational realm. Manufacturing constraints are not considered, such that the manufacturability remains questionable. The algorithm is shown in brief in Figure 2.9 but will be addressed more extensively in Section 5.2, as it will be used as a basis for this research.

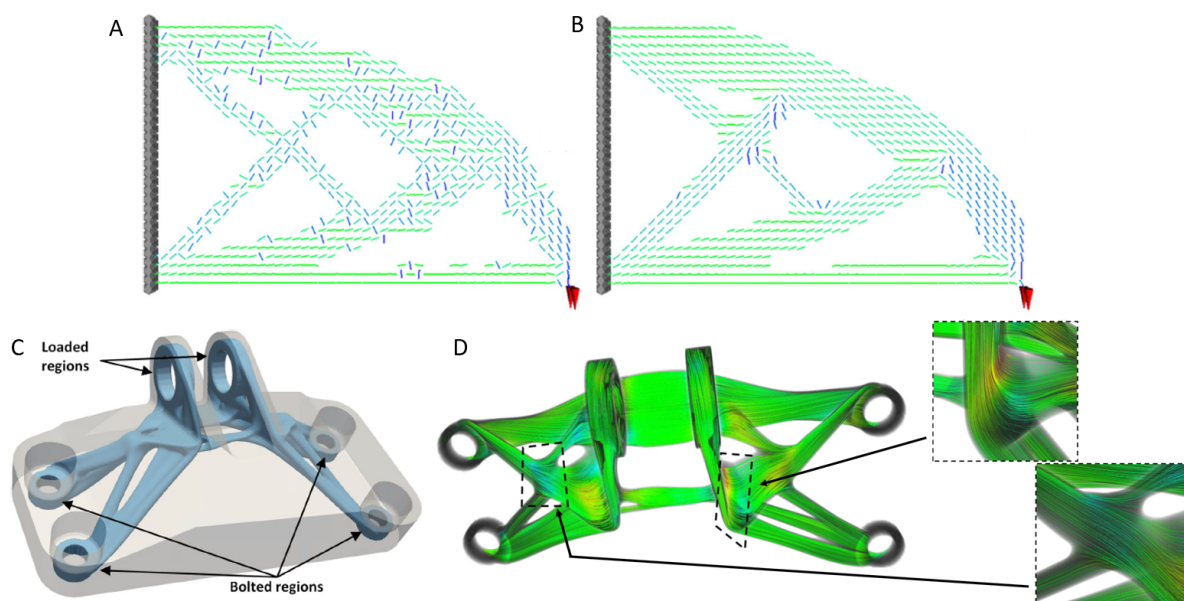


Figure 2.9: Topology optimization algorithm including optimal fibre orientation. A: 2D cantilever beam without filtering for smooth fibre orientation variation. B: Cantilever beam with smoothly changing fibre orientations. C: 3D case, a topology optimized bracket. D: Fibre direction within the bracket, which are smoothly varying.

3

Thesis definition

In this chapter, the full outline of this thesis project is explained. First, the rationale behind this thesis is explained in Section 3.1. Here, the identified research gap is given, the resulting research objective is defined and the scope of the thesis project is set. This is followed by the research questions which are given in Section 3.2. Finally, the part used as a case study is presented in Section 3.3 and a simplified planning is given in Section 3.4.

3.1. Research gap and objective

The focus is gradually changing in the FFF printing world, shifting from rapid prototyping to structurally demanding applications. In the previous chapter, a gap in the literature has been identified. A number of Topology- and Anisotropy- Optimization (TAO) algorithms have been developed in the recent years. Their manufacturability has either not been taken into account or trade-offs in fibre direction had to be found, leading to sub-optimal experimental results. Furthermore, to date only 'conventional' materials (PLA, ABS) have been used to test out these TAO algorithms, while the newer high-strength anisotropic FFF materials (CFRP filament, LCP) would be more beneficial to this printing method. No dedicated research so far has focused on using materials which display a superior fibre-like behaviour to print a three-dimensional part generated by a TAO algorithm along non-planar stress lines. LCP is chosen as the ideal material for this, since it exhibits similar properties as CFRP filaments, but has very high shaping freedom and is fully reusable. Therefore the research objective is defined as:

“To achieve structurally improved FFF parts without changing their material and shape through stress-aligned 3D printing with highly anisotropic liquid crystal polymers.”

Additionally, in the most recent TAO algorithms discussed in the literature, the individual stress lines are not truly stress-aligned. These algorithms do not really transition away from the curved-layer approach. The manufacturing sequence is generated to have the inter-layer surface close to the smallest principal stress direction. In order to achieve true SA printing, non-planar and non-layer-wise printing has to be utilized. This means a new improved printing strategy is needed.

In order to develop and implement this non-planar printing strategy, a 3D Printer with 5 DOF is chosen. This overcomes a lot of limitations conventional 3 DOF FFF printers have, as was also highlighted in the literature study. Multi-axis FFF is a new research field within the faculty of Aerospace Engineering. Therefore, this project will also function as a kick-start to 5DOF printing at the 3D printing lab. This will be done by improving an already-existing printer, investigating its limitations, documenting findings and best practices.

One crucial milestone in implementing the stress-aligned printing method is to build a workflow for generating code for 5 DOF printing, since commonly known slicers for planar 3DOF printing are unusable. A completely new method of path generation has to be developed, which will determine the success of this project. A lot of choices towards this printing strategy have to be made. For instance, considerations such as how to order the lines when they do not form layers, how to orient the nozzle,

how to make sure the printer does not crash into the already printed section, need to be implemented. For these reasons, the final algorithm for converting the stress lines into printer code is considered a primary result of this research.

As a consequence, the sub-goals to achieve the main objective can be described twofold:

1. To develop a fully functioning, versatile and robust 5DOF printer.
2. To develop an algorithm that takes a stress analysis as input and outputs a printing program for a 5DOF printer.

When these two sub-goals are achieved. One can use the 5DOF printer and the stress-aligned print path algorithm and print with it using LCPs, which will result in achieving the main thesis objective, printing high performance FFF parts.

3.2. Research questions

To find out how much potential improvement SA printing of LCPs really has, one has to compare it to a baseline. This baseline has to be printed using the conventional method of 3D printing; planar, layer-wise printing. Thus the main research question is defined as:

What is the strength increase in FFF parts obtained by using stress-aligned non-planar printing versus planar printing using Liquid Crystal Polymers?

To find an answer to this question the research is split up into two sub-questions. This also divides the research into manageable work packages.

1. Given a printed part with load case, what is the ultimate strength when using planar FFF with LCP filament?
 - What are the ideal printing parameters for LCP while printing said part?
2. Given a printed part with load case, what is the ultimate strength when using non-planar stress aligned FFF with LCP filament?
 - How are the stress lines running within the given part and load case?
 - What is the optimal printing sequence and strategy for printing along these stress lines?
 - How can this printing strategy be translated into a program for a 5-axis printer?

3.3. Scope: case study bracket

For this research, it was chosen to focus on a case study part to investigate the potential benefits of SA printing. Additionally, an extensive structural analysis to obtain stress lines in a part is outside the scope of this project. The research by Schmidt et al. (2020) provided a solution to both these issues, which was extensively discussed in Section 2.2.3.

The choice fell on the bracket that is used in the GrabCad & General Electric (GE) Topology optimization challenge (GrabCAD (2013)). This challenge was aimed at redesigning a bracket used in one of GE's jet engines, optimizing it for use with additive manufacturing techniques. The challenge ended in 2013, but the part is still commonly used to this day in research to show results for TO algorithms, as was the case in Schmidt et al. (2020). This yielded a topology optimized bracket which includes the optimal direction for fibres in the part. The steering radius of these fibres is limited such that the fibres run continuously without irregularities, making it ideal for FFF. The data of the research was kindly provided by the authors of this research paper. The resulting case study part can be seen in Figure 3.1, the fibre direction is also provided as a vector field, which will be shown later in Figure 5.5. Henceforth the case-study part, this topology and anisotropy optimized GE & GrabCad challenge bracket, will just be referred to as 'stress-aligned (SA) bracket' or 'bracket'.

Since the Grabcad & GE challenge is a structural optimization challenge, it also provides design requirements in the form of four load cases it should be optimized for. These four load cases are

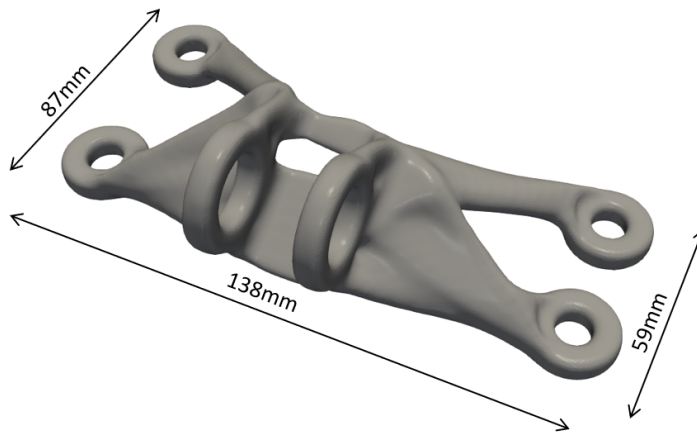


Figure 3.1: The case study part for this research. A topology optimized bracket by Schmidt et al. (2020)

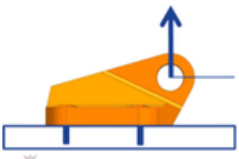
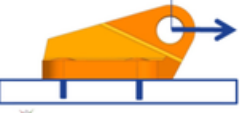
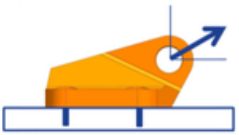
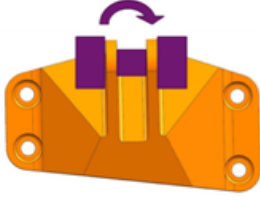
<p>Load Conditions 1</p> <p>Static</p> <p>Vertical</p> <p>8000 lbs up</p> 	<p>Load Conditions 2</p> <p>Static</p> <p>Horizontal</p> <p>8500 lbs out</p> 
<p>Load Condition 3</p> <p>Static</p> <p>42 degrees from Vertical.</p> <p>9500 lbs out</p> 	<p>Load Condition 4</p> <p>Static Torsional</p> <p>Horizontal plane at centerline of clevis.</p> <p>5000 lb-in</p> 

Figure 3.2: Load cases of the Grabcad & GE bracket optimization challenge. For this project load case 3 was chosen. Extracted from GrabCAD (2013).

given in Figure 3.2. Due to time constraints printing brackets for all four load cases of the topology optimisation challenge was not possible, hence only one load case is tested in this research. Load case 3 was chosen, since this is the load case with the highest force requirement, thus making it strongest in this direction. It must be noted that by choosing only one of the load cases, while the TAO algorithm optimises the bracket for all four load cases, the stress-lines do not always lie in the most optimal direction for load case 3. Also, it is not expected to reach the required load of 9500 lbs (42kN), since this challenge was meant for a titanium bracket. The particularity of this part is the fact that it is not symmetric due to the non-symmetric placement of the lower attachment points. This will result in some non-symmetric load paths that should not pose a problem for 3D printing. In summary, this bracket is identified as an optimal first case study to develop and evaluate the SA printing strategy.

3.4. Road map

To structure the project three work packages were defined. The first phase is to improve the 5-axis printer, whose modifications will be discussed in Chapter 4. These modifications are needed to enable a larger freedom of motion of the 5-axis printer. This is done first such that down-time would be minimized, and eventual lead-time delays do not cause delays in the project. Simultaneously the coding is started on Rhino and Grasshopper (Robert McNeel and Associates (1993)), as it is the chosen program to make the G-code, which will be discussed in Chapter 5. Then, to finish this phase of the project, a few simple 3-axis and 5-axis parts will be printed. This will serve as a test for the new printer but also for the skills acquired in generating 5-axis G-code in the meantime.

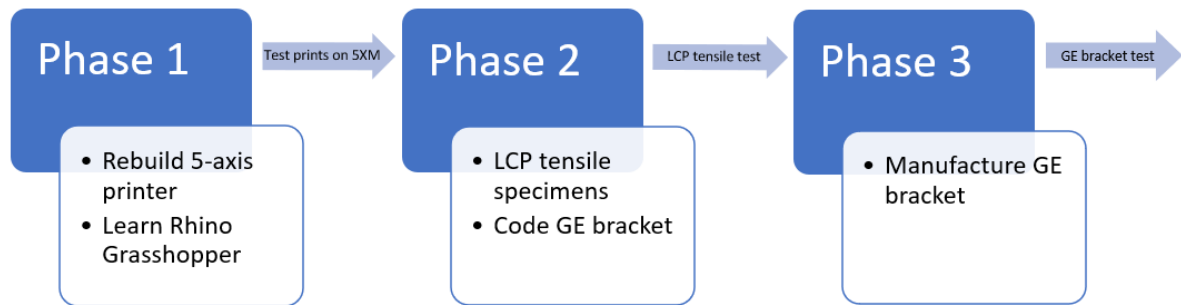


Figure 3.3: Road map for research project divided into 3 major phases.

The second phase consists in manufacturing a batch of small tensile specimens of LCP. Along with gaining experience with using the material, a lot of knowledge can be gathered about optimal printing parameters. Simultaneously in this phase, the algorithm for generating the G-code for the SA bracket is developed. This phase ends with tensile tests of the LCP specimens and a finished G-code for the SA bracket.

In the final phase, the SA bracket is manufactured, in a highly iterative process of debugging and improving the G-code generation algorithm. At the same time, a planar printed bracket is manufactured. This phase ends with the tensile test of both brackets. The road map is shown in brief in Figure 3.3. This way, the project is brought to a successful end in a timely manner.

4

Experimental setup

All the work in this thesis was conducted in the Delft Aerospace Structures and Materials Lab (DASML) at the TU Delft, where the Shaping Matter Lab (SML) is situated. First, the 5-axis printer will be discussed in Section 4.1, which has undergone some heavy modifications. Then the other printers used in this project are presented in Section 4.2. And finally, Section 4.3 will elaborate on the test setup for the tensile tests for the tensile specimens and the bracket itself.

4.1. Five-axis 3D printer

For printing in a true stress-aligned fashion, a conventional 3-axis printer is not sufficient, thus, a 5-axis printer is needed to increase the dimensional freedom. The Shaping Matter Lab owns a 5-axis machine that is used for this project, and it will be presented in this chapter. The first subsection explains the hardware side, where a lot of modifications were done. The second subsection contains an explanation of how the printer is controlled.

4.1.1. Hardware

The machine used for this project is the 5AXISMAKER (5XM). Made by 5AXISWORKS LTD (2020), this machine is designed as a desktop size 5-axis Computer Numerical Control (CNC) milling machine but features 3D printing capability by swapping the milling end out for a hot-end with nozzle. An extruder is supplied to be mounted on the frame, using a Bowden tube setup to feed the filament through the nozzle.

The coordinate system the 5XM uses is illustrated in Figure 4.1. The A-axis is the extruder stepper motor and the B and C axes are the X-axis rotation and Z-axis rotation respectively. The X-Y-Z axes are used to position the print head including B and C axis in a cartesian coordinate system.

While this setup is workable, many limitations were noticed upon first use. It is known that the pressure that an extruder in Bowden tube configuration provides is less constant and less powerful than a direct drive setup (Gibson et al. (2010)). Especially with LCP filament, where the needed extrusion force is relatively high, and a constant extrusion rate is very important for the mechanical properties (Houriet (2019)) a direct extrusion drive is preferable. It was chosen to swap the original extruder setup for a Hemera direct drive setup (E3D Limited). The original heating cartridge ran on 220V AC, which is very uncommon and replacement parts are rare. Therefore, the wiring in the power supply unit (PSU) was altered such that the heater would run on 12V DC, which is readily available since the homing sensors on the 5XM utilize the same voltage. Finally, to increase the clearance of the nozzle during 5-axis printing, a special long nozzle was fitted. The difference in clearances is visible in Figure 4.2. This added a lot of thermal mass and surface area to the hot-end so additional insulation was provided to make sure the required temperature could be reached. A 40W heating cartridge was mounted, with a maximal attainable temperature of 350°C, which is well above what is needed for LCP.

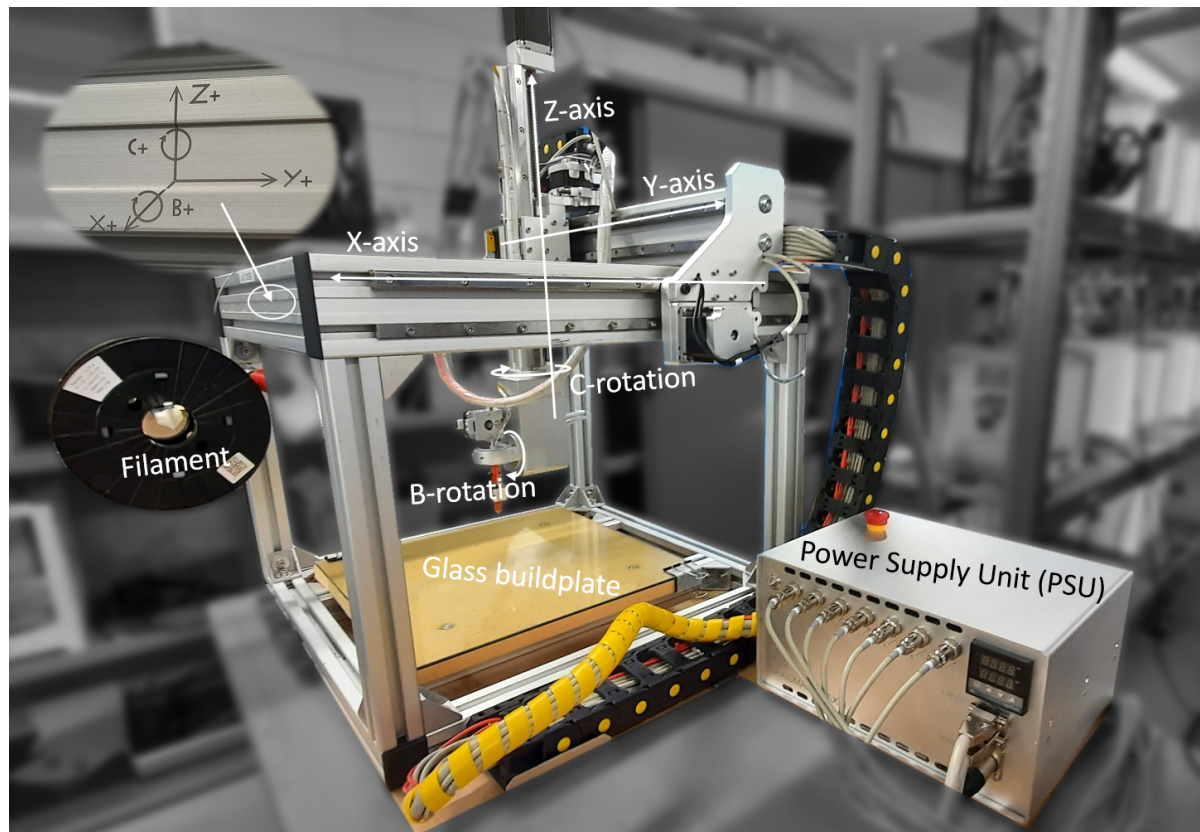


Figure 4.1: The 5AXISMAKER in the Shaping Matter Lab. 5-Axis FFF printer used for this research.

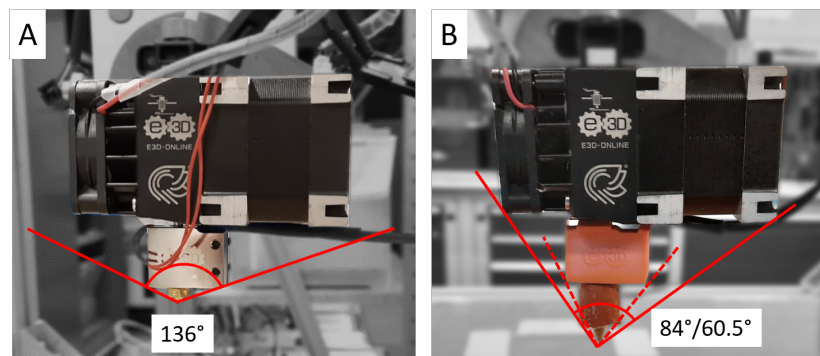


Figure 4.2: Extra printing clearance given by attaching the long nozzle. The insulation to maintain higher temperatures can also be seen.

A second limitation can be attributed to the way the printer is wired. The cables running to the print head and the extruder get tangled up when rotating the C-axis more than $\pm 180^\circ$. This makes continuous spiral prints impossible and limits the available shaping freedom. A solution for this is to install a slip-ring connector, which passes through signals while having full rotational freedom.

To select the right slip ring an investigation into the wiring has been executed. The slip ring chosen was the SRH3899-24S from Franke GmbH. This slip ring features 24 signal connections, which is a little more than needed, leaving room for possible future additions. It also has a relatively small size, as to not limit the moving space of the 5XM too much. The wiring was altered such that there are two connectors on each side of the slip ring; one for everything inside the print head (B & C axis stepper and homing sensors), and one for everything on the Hemera (extruder stepper, heater, thermistor and fan). The pin-outs were designed in such a way that the slip ring could be bypassed at any time if the need arises. The wiring diagram and the pin-outs of the connectors can be found in Appendix A.

This slip-ring is mounted around a custom-designed aluminium extension of the z-axis, which makes assembly and disassembly of the slip ring easy. It is also stiff and lightweight, such that it would not add extra vibrations to the already heavy print head. The downside of this modification is that the available z-height is decreased. Therefore the outer frame of the 5XM was enlarged by 10cm, about the same as was lost by fitting the slip ring. The final modifications to the print head can be seen in Figure 4.3.

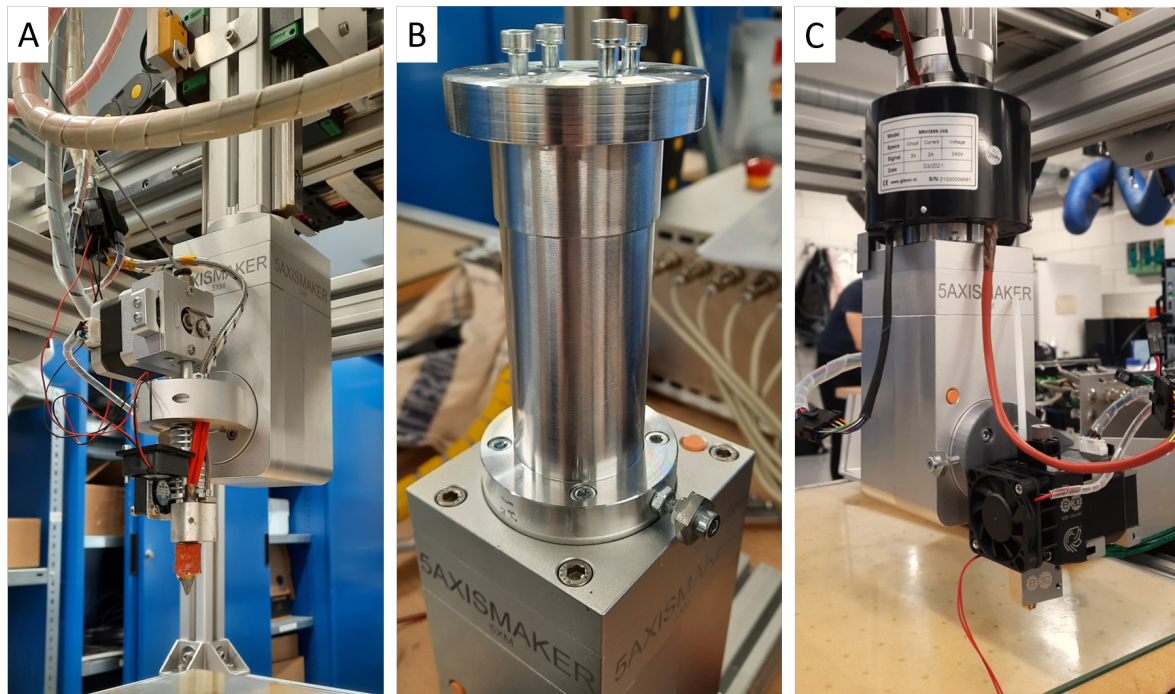


Figure 4.3: Modifications to the 5XM. A: Before modifications. B: Custom z-axis extension to attach the slip ring. C: Slip ring and new Hemera extruder fitted.

The 5XM comes without a build plate, just a frame to attach things to. This is an advantage in the sense that one can attach any kind of structure to print on, from flat plates to complicated moulds. However, it also does not come with a heating system for a build plate or mould. This is needed since a heated bed aids adhesion and prevents warping of a printed part (Gibson et al. (2010)). First, a control box was built for the heater system. It was chosen to give it both the options to run on 24V DC and 220V AC, to make it widely applicable in the future. The control was done by a Proportional-Integral-Derivative (PID) controller, the InkBird ITC-100. The inner layout of this control unit can be found in the Appendix in Figure A.3.

The 5XM was then fitted with a glass plate of size 400x400mm, with a 220VAC 1200W heating pad attached to it, providing ample space and heating power for future applications.

With this improved 5XM, a range of prints were successfully made to test the possibilities with this printer. Figure 4.4 shows the results of one of the tests. This print would not have been possible with a 3-axis printer.

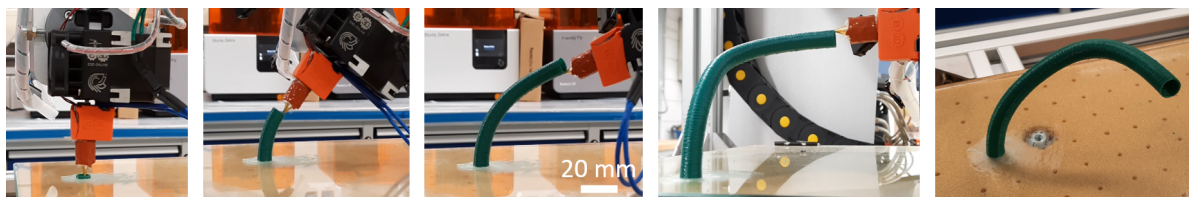


Figure 4.4: Curved tube printed by the 5-axis printer as a full integration test of the machine.

4.1.2. Control

The 5XM is run by a dedicated 6 axis control board developed for the machine and controlled using the CNC software Mach3. The software is responsible for translating the print trajectories given in the form of g-code to motor outputs and calculating synchronized movement of the axis.

Once the machine is powered up, the first step is to calibrate it. The software does not know the current status and location of the axis of the machine when it started. A short script needs to be run first to slowly move the X-Y-Z axes to their respective end stops, which are mounted to the frame in the form of a couple of inductive proximity sensors. After which Mach3 knows the position of the axes and sets them to 0. A similar operation is done for the B and C sensor, but these are not situated at a straight position. It measured how large the angle between the sensor trigger position and the straight position was using a micrometre, which was then hard coded into the calibration script. These angles were 59.03° and 31.90° for B and C respectively. After this script is run, the machine is in its 0 position and Mach3 can now be used to control the axes.

Then a second script will be executed to set the origin for the G-code that will be run. For a print on the heated glass plate, this was chosen to be a nozzle position of 0.1mm above the upper left corner, when the B and C axes are zero. But for any other print, this can be different. The bed and nozzle temperature are controlled separately, with both of them having their own PID control unit, where the temperature can be set.

4.2. Other printers

A couple of components that were printed during this project are not printed on the 5XM, but rather on a conventional 3-axis printer. The parts that are printed from PLA were printed on a Prusa MK3S. LCP parts were printed on either an Ultimaker 2+ Extended or a Prusa Mk3S. Both of these printers are slightly modified to enable LCP printing. All printers were built in previous research projects at SML and were reused here.

4.3. Mechanical tests

To test the structural properties mechanical tests were performed. These were conducted on the tensile benches available inside DASML. A Zwick-Roell 20kN test bench is a displacement controlled tensile test machine which can support a wide range of fixtures. For this project, two fixtures were needed.

For the LCP tensile test specimens, hydraulic grips were used. These hold the specimen in the bench by applying very large clamping forces on the end of the specimen. The clamping pressure can reach up to 100bar. To increase the grip even more and to prevent the specimens from crushing they were protected by tabs.

To answer the final research question the bracket was also tested under the given load case. For this, a custom fixture was designed. This fixture should be able to place the bracket under the test bench at the required load case as given in Figure 3.2. Which means it is fixed under a 42° angle with respect to the tensile force. The fixture is bolted to the tensile bench, and on the other side contains the bolt pattern of the bracket. The final design and fixture can be seen in Figure 4.5. The top lugs are attached to the bench with a pin through both of them, and some bolts and washers prevent sideways sliding of the bracket. The fork that supports this pin is attached to the top of the bench by two swivel joints, such that it can adjust its orientation to the bracket and load both lugs equally.

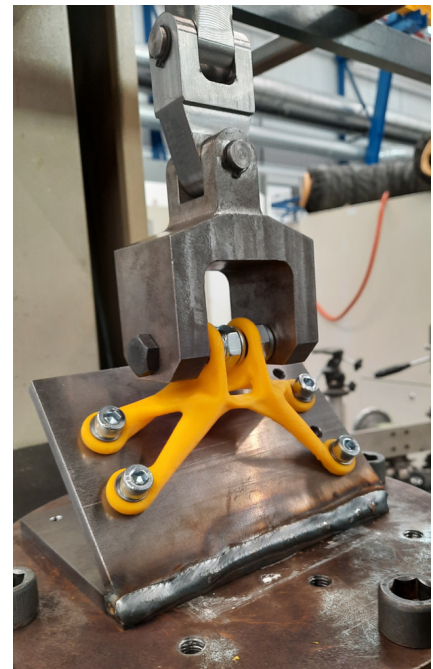


Figure 4.5: Test setup with an example PLA bracket installed.

5

Results - Path generation

One crucial aspect of this research was to control the printer in such a way that it prints along the stress lines. The standard used for CNC machines is the G-code language. This is a large text file with each line consisting of a single command. All the lines which command the printer to move one or more of its axes start with the letter G. Any other (non-moving) command starts with the letter M. A small example code is given below in Table 5.1, with an explanation of each line.

G-code is a human understandable coding language, which makes it possible to write simple G-codes manually. However, for projects consisting of thousands of commands, generating the G-code for a CNC machine is usually done by a piece of Computed Aided Manufacturing (CAM) software. For 3D printing this software is the slicer, since it slices the part into layers for printing. While the existing slicers are adequate for traditional use of 3-axis printer, no such software exists for 5-axis printers yet. For subtractive manufacturing, 5-axis software does exist but only in complicated and expensive software packages, which are mostly unusable for additive manufacturing.

For this project, a 5-axis G-code is needed, but a method for generating it had to be developed. It was chosen to generate the G-code using Rhino and its plugin Grasshopper (Robert McNeel and Associates (1993)). This is a Parametric CAD software, which is very suitable for integrating coding with CAM/CAD. The process of generating this G-code is explained in this chapter.

The printing of the SA bracket was split up into parts; The supporting structure/mould (Part A, Section 5.1), the main body with bottom fastening points (Part B, Section 5.2) and the upper lugs (Part C, Section 5.3). It is illustrated in Figure 5.1. The support structure was printed conventionally using a 3-axis printer. Part B was analyzed and printed along the stress lines given by the optimization as in

Table 5.1: Example G-code with explanation of the lines

G-code	Meaning
G0 X0 Y0 C0 B0	Move the printhead to X=0, Y=0, C=0 and B=0 with travel (maximum) speed
G1 F100 A30	Move the extruder axis to A=30mm with a feed speed of 100mm/minute
G92 A0	Save/set the current A axis position as A=0. (calibrating the A axis)
M8	Switch on main cooling Fan (machine specific)
F800	Set the feed speed to 800mm/minute for all following G1 moves
G1 X254.74 Y149.08 Z3.76 A0.17	Move the printhead to X=254.74mm, Y=152.58mm, Z=3.76mm, A=0.17mm
G1 X254.21 B12.34 C117.50 F500	Move the printhead to X=254.21mm, Y=12.34°, C=117.50° with a feed speed of 500mm/minute

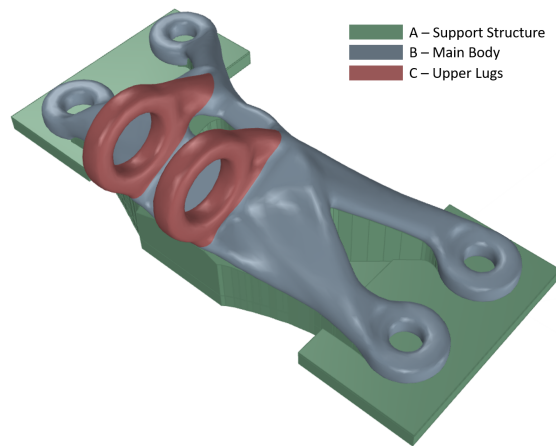


Figure 5.1: Division strategy for printing the SA Bracket.

Schmidt et al. (2020), and therefore the focus lay on this part. Part C was printed on a 3-axis printer using an orientation optimal for strength.

5.1. Support structure

In the Section 2.1, it became clear that supportless printing is widely studied, and that LCP is a good candidate for this method. However, in this thesis supportless printing was not the aim and would not add to the final strength of the part so it was chosen to print the bracket on top of a supporting structure. This support formed the mould for the 5-axis print of the bracket itself.

The support structure was printed on a conventional 3-axis printer using PLA. The LCP was printed at a much higher temperature ($> 290^\circ$) than the glass transition temperature of PLA. This might have caused the support to become too hot and warp. Therefore, small tests of LCP printing on top of PLA were conducted. A small $30 \times 30 \text{ mm}$ square of LCP is printed on a 2 mm thick PLA plate, which did cause small amounts of warpage. This can be seen in Figure 5.2. However, when the support was increased in thickness the warpage became less severe. And while printing the SA bracket, the lines were not so compact such that the heat was more easily dissipated. The LCP also released from the PLA support easily after printing.



Figure 5.2: Test print of LCP on PLA. Small warpage of the PLA is visible. Releasing the LCP square was no problem

The bracket support was generated in Grasshopper/Rhino by extracting the projected volume downwards from the bracket. To enable easy printing of the attachment points, two flat pieces were added on the sides. The support was printed using a Prusa MK3S with PLA. The resulting support structure can be seen in Figure 5.3.

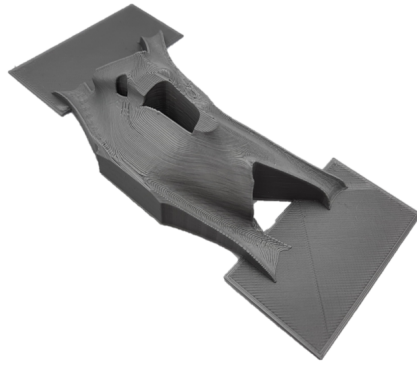


Figure 5.3: Finished PLA support structure/mould to print the bracket on.

5.2. Main body

The main body was printed using the stress-aligned slicing method. Therefore, for this part, the focus was on the slicing algorithm, while the other parts were used simply to make manufacturing and testing of the body possible. The algorithm can be split up into 7 steps. These are summarized in Figure 5.4 and will be fully explained in the next 7 subsections.

5.2.1. Generate stress lines

The output of the optimisation by Schmidt et al. (2020) was provided in the form of a vector field. To interpret this vector field the TAO algorithm has to be explained more in-depth. The design space for the bracket was divided into voxels with a resolution of $x=95$, $y=59$, $z=36$. This results in each voxel having a size of $2 \times 2 \times 2$ mm. The optimization then determines the density for each voxel, incorporating the optimum direction for anisotropy in that voxel to minimize compliance. These directions are limited to a certain radius of curvature, such that they form smoothly varying fibre directions. The vector field provided is thus a 3D array of vectors which are all scaled to their density. This means that outside the final geometry, the vectors have a size of 0. Inside the geometry, they are 1 and at the boundaries, they are between 1 and 0. A visualization of the vector data is given in Figure 5.5.

To convert this data into printable lines, the open-source program ParaView was used (Kitware (2020)). Its main function is to perform data visualisation, as well as create figures and renders of data. The vector field could be integrated using the 4th order Runge-Kutta method (RK4) to obtain flow lines. This function is called the 'Streamtracer'. It randomly seeds a specified sphere with particles and then integrates these particles as they move through the vector field. The RK4 integration is performed both ways (forward and backwards), to get full streamlines from start to end of the vector field. A number of integration parameters had to be specified, such as the number of seeds, particle lifetime etc. The used parameters can be seen in the appendix in Figure B.1. The parameters were tuned such that the streamlines were spaced tightly. The spacing was smaller than the nozzle diameter, and thus resulted in too many lines to physically print. What this enabled is selecting the right line density by randomly deleting a couple of lines, without having to generate them in ParaView again. One effect of the vector field not having discrete boundaries but a transition area means that the RK4 integration does not always stop exactly at the boundary of the part but overshoots or undershoots it by a small margin. This is not a big problem but had to be taken into account in subsequent steps in the algorithm. The resulting streamlines are shown in Figure 5.5.

These streamlines will henceforth be referred to as the 'stress lines' since it makes it more intuitive to understand what they represent, making the rest of the report easier to read. It must be noted that they are not actual lines of stress, but rather lines that represent the optimum fibre direction for the four load cases described in Section 3.3.

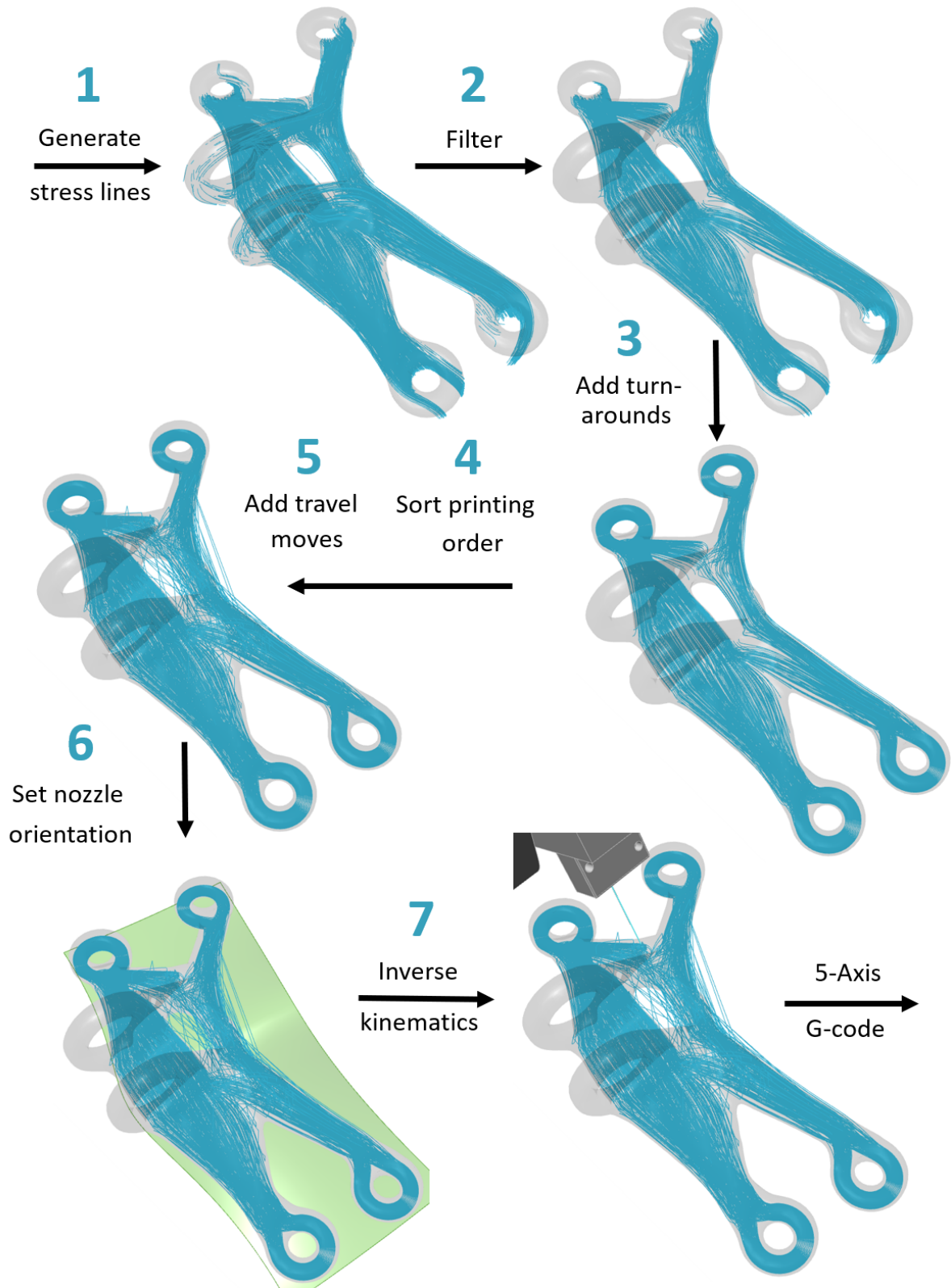


Figure 5.4: Complete workflow for generating the full print path of the SA bracket. 1: Stress lines are generated from vector field in Paraview, 2: Invalid lines are filtered out, 3: The attachment points are added connecting all the stress lines on one side, 4: The print lines are ordered such that they will print bottom up, 5: Travel moves are added making it one continuous print path, 6: Normal direction for the print head is determined, 7: Inverse kinematics determines 5XM axis position which is written into a G-code file.

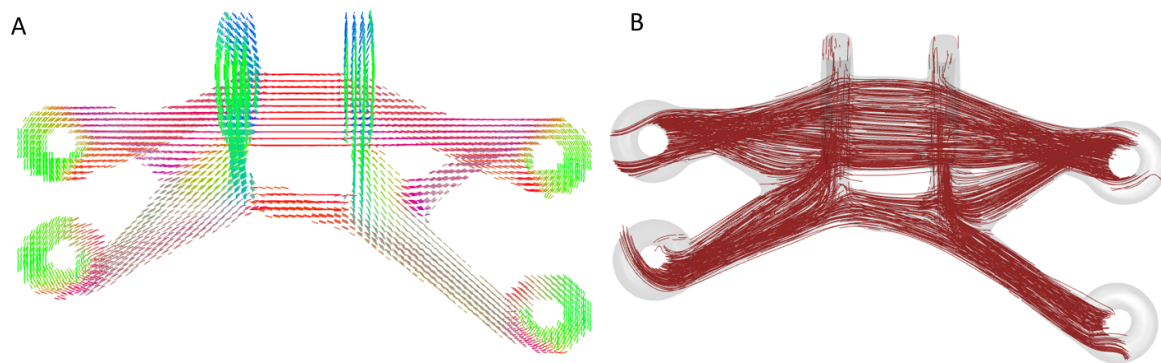


Figure 5.5: A: Visualisation of the vector field generated by the algorithm in Schmidt et al. (2020). Coloured according to curve radius. B: Resulting stress lines after RK4 integration of the vector field by ParaView

5.2.2. Filter unusable print lines

From this point forward the algorithm is written in Grasshopper/Rhino. Therefore, the first step was to export the data from ParaView into Grasshopper. The raw data comes in comma-separated values (.csv) format and was converted back into individual lines. These lines contain a number of errors, so the following filtering and trimming operations were done:

- **Delete short lines** - All the lines shorter than 45 mm are deleted, to reduce the number of lines that do not contribute significantly to the final strength, thus decreasing the coding complexity at a later stage.
- **Trim lines colliding with support** - Due to the method of streamline generations, some streamlines may lie slightly outside the geometry of the part as explained before. While this is not an issue for lines that protrude above the part, when this protrusion is below the part, it will mean that it is printed inside the support structure. Therefore, these lines were trimmed.
- **Decrease line density** - The lines exported from Paraview have a very high density, too many to print. Therefore a percentage of the lines were randomly deleted. This way one can tune the line density without having to export a new .csv file from Paraview every time, enabling quicker iterations.
- **Trim too high lines** - Some lines continue into the position of the upper lugs. These are far away from any other structure and would be printed in mid-air, which is not feasible. To prevent this, all the lines above a certain height were trimmed.

Figure 5.4 shows a comparison of the lines before and after the sifting operations.

5.2.3. Turn-around sections

At the four lower fastening points, the stress lines did not conform to the geometry of the part as can be seen in Figure 5.5. This made the points unsuitable for usage as fastening points, and needed to be addressed. Therefore, custom print lines had to be designed there.

For optimum strength, the print lines have to be continuous. Therefore, it was chosen to connect two print lines with a 'turn-around' section. All the stress lines were trimmed at the attachment points. Then two lines were connected by a turn-around section as follows. One was chosen as an incoming stress line, which then transitioned into the semi-circle around the fastening hole and was connected through an additional transition the outgoing stress line. The transitions were generated by a spline function, which avoids kinks and ensures a smooth transition. The combination of an incoming line - transition - semi-circle - transition and outgoing line formed a single print line as illustrated in Figure 5.6.

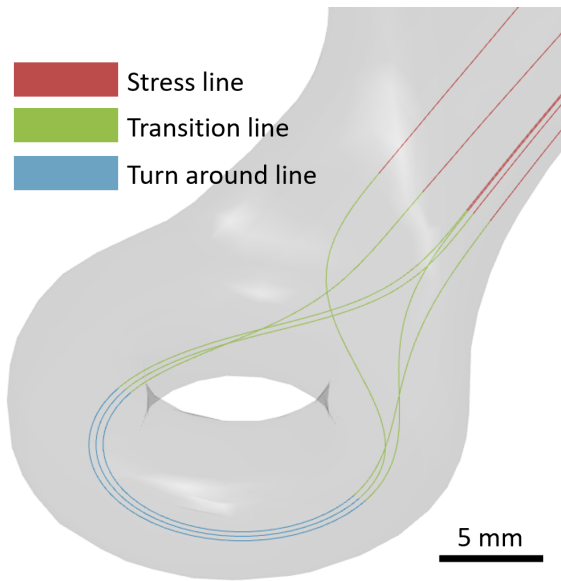


Figure 5.6: Six stress lines connected by a turn-around section into three continuous lines

These turn-around sections then formed the geometry for the fastening points. These were neatly ordered, with the first line being at the inner radius, increasing the radius by 0.4mm (chosen equal to nozzle diameter) for each turn-around section. When the outer radius was reached, a new layer was printed on top of it.

This method also relates to another issue commonly discussed when printing parts that need to be able to withstand loads, namely how to print junctions in the geometry. In the transition from the body to the fastening point, the geometry splits into two, meaning each line either goes left or right. It could seem logical to split the lines down the middle and let them run left and right respectively, in a similar manner to how most open-hole test specimens look. However, this would create an obvious weak point in the middle where the geometry could split when subjected to a mode 1 force. This is especially true with highly anisotropic material, where the transverse bond between the lines is very weak. By not splitting them in the middle but randomly dividing them over the two sides the transition piece becomes very intertwined.

This is similar to how transitions are handled in nature, taking inspiration from tree forks. These are huge junctions in trees having to withstand a high mode 1 force trying to open up the junction, especially under stormy conditions. The wood grains in these junctions break free from their parallel paths and become highly intertwined, creating mechanical interlocking and making that area less anisotropic than the trunk of the tree (Slater et al. (2014)). This mechanism can be replicated when 3D printing. Especially when using a 5-axis printer which enables lines to cross over each other making them not layer-bound. By randomly choosing if a line goes left or right the transition area will become more isotropic, strengthening it.

5.2.4. Sort printing order

Looking back at planar printing, where everything is neatly ordered in layers, identifying what to print first is trivial: starting from the bottom, working upwards. In the 5-axis case, this triviality is not present. The lines do not form layers, and the bottom is not well defined. However, one can approach a similar bottom-up method by sorting the lines. To do so, a certain location on the streamlines must be chosen to sample the z-coordinate (height) of the streamline, and print it in order of increasing height.

First, all the lines were sorted into four groups, one for each of the attachment points. This revealed an interesting fact of the stress lines. Almost all stress lines ran through one of the attachment points only. Roughly 3% of the stress lines run from one attachment point to another. This is a result of how the streamlines were generated in ParaView. When the geometry becomes more narrow, meaning cross-sectional area decreases, some lines stopped. This was done to maintain the same line density. Of course, this also meant that the other way around, when the

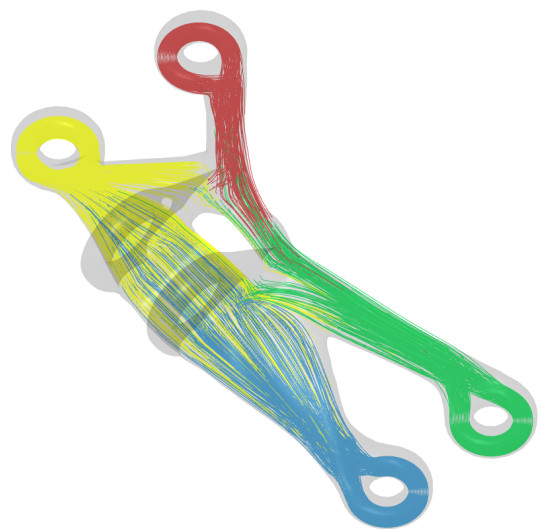


Figure 5.7: The stress lines colour-coded into their respective attachment point group.

cross-sectional area increases more lines appear. Since the seeds for these lines were randomly distributed, a larger cross-sectional area also means that more lines were seeded there. That is why lines that cross a certain attachment point very often did not 'survive' to the next attachment point, since the cross-sectional area decreases when it approaches an attachment point.

The four resulting groups are shown in Figure 5.7. Where it is clear that the lines from attachment points 1 and 2 (blue and yellow) form an area where their print lines intertwine with each other. The same can be said for points 3 and 4 (green and red). However, between the front and rear attachment point few lines link them together. This is a result of how the stress lines run under the given load case. Stress has to travel from the upper lugs to the bottom attachment points, and not from attachment point to attachment point, hence few lines exist between them. These two parts were thus to be linked together when the upper lugs are fastened (see Section 5.3).

This discontinuity between the front and rear stress lines provides a good way to order the printing lines. First, the two front stress line groups are printed, alternating between left and right. Then, the same was done for the two rear groups.

Now that the order of the groups was determined, it was necessary to be more specific on how the lines are sorted within one group, since they are still unordered there. As mentioned before, these are all trimmed at their attachment point where the lines transition into the turn-around section, forming the intertwined junction. To let all the lines cross over each other properly, they were ordered in height at the points where they are trimmed. This means that the bottom-most line was the first incoming stress line, and the second bottom-most line was the first outgoing stress line. This process was repeated for all stress lines in a particular group. Since the attachment point groups do not have the same amount of stress lines, the thickness differs at each attachment point, determined by the number of lines.

5.2.5. Travel moves

Now that all the lines that need to be printed were complete, the last step to obtain the full path for the print was to connect all the lines with travel moves. These are moves solely for moving the nozzle from the end of one line to the beginning of another. In planar printing, these travel moves are again trivial. The nozzle stops extruding material when the print line is done, travels to the start point of the next print line in a straight line and continues printing there. In 5-axis printing, more thought has to go into how to smartly program these travel moves. Travelling in a straight line does most of the time not work, since that would mean that the nozzle would crash into the already printed part, or into the support structure.

The simple solution would be to make print lines that are always higher than the supporting structure. By travelling straight up after a print line is finished, then horizontal to the new start position and then straight down to the start point of the next print line. This method was tried, but it exposed a problem. The adhesion between the PLA support and the LCP print line was very weak, weaker than between the hot nozzle and the print line. This means that when the nozzle started moving upwards, it pulled the print line with it and off the support. This immediately led to a failed print. So another method for connecting the print lines was devised.

A better method is to have the travel move run horizontal, like in planar printing. This cleanly shears off the hot filament from the printed line, leaving it in place. Yet horizontal movement is not always an option, since it would run into the support. For that reason, the travel moves run parallel to the supporting structure, essentially following the contour of the part. Still, the start point and endpoint of a travel move are not at the same height, where height means Z-distance from the support. A choice thus has to be made on how high this travel move should be. There are two options, illustrated in Figure 5.8:

- **Lower Option** - When the lowest of the two points is chosen, the discrepancy between the two heights is filled with a horizontal travel move. This is good for shearing off the filament from the printed line. It could however place the travel move at a height that is filled by previously printed lines, leading to a crash.
- **Higher Option** - When the highest of the two points is chosen, the discrepancy between the two heights is filled with a vertical travel move. This is bad for the shearing behaviour and might pull the print line with it. Yet it is a safer option since it does not place the travel move where a previous printed line could be.

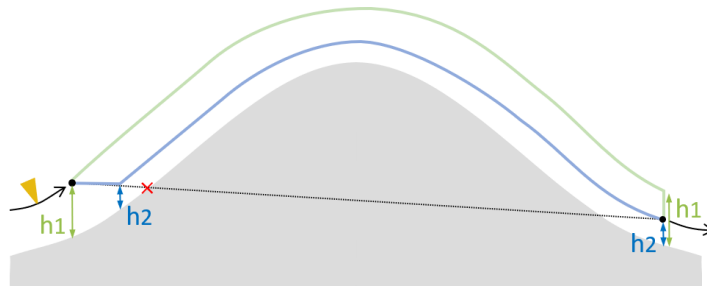


Figure 5.8: Lower (Blue) and Higher (Green) travel move options.

Both options were tested and it was found that in the lower option the nozzle would often travel through already printed lines, leading to a crash. Therefore the second option is chosen. To overcome the issue of the printed line possibly being pulled off the support, it is decided to not stop extruding during these travel moves. This does leave a visible travel move in the print, but it is deemed the best option for better manufacturability. As a bonus, these travel moves are close to the most direct route the nozzle can take between two print moves, which saves printing time.

This method was implemented in the path generation algorithm as follows. For each travel move, the supporting structure is raised to the height of the highest point (either start or end). A vertical surface is generated from the line connecting the start and endpoint. The intersection between this surface and the raised supporting structure is obtained, which resulted in a line which is the travel move. A number of post-processing steps were needed to finalize them.

- The direction of the intersection line is always towards the positive x-direction. Some lines needed their direction flipped. This is done by generating a vector between the start and endpoint of a travel move and using that vector as a guide for the direction of the travel move.
- When a travel move goes through an area that does not lie above the supporting structure, the intersection calculation would also yield the vertical wall from the support. The travel move should not travel down that wall, since this will result in a crash, so all the vertical segments are trimmed off. This was done by sampling the lines at 1mm intervals, and deleting the sections where the direction was in the Z-direction.
- Sometimes a travel move would intersect the support twice, when it traveled across a hole in the support. This resulted in the travel move consisting of two separate line segments. In that case a straight line between the two segments was added.

In Figure 5.4 the final result of the print path is illustrated complete with travel moves.

5.2.6. Print head orientation

On a 5-axis printer, one extra step is needed after determining the complete print path when compared to a 3-axis printer. This step is to determine the orientation of the print head, and with that the nozzle during the print. Here, the aim is to prevent crashes by having the nozzle oriented normal to the print path.

A similar approach as the travel moves was taken. Where the supporting structure was used as a guide. Since all the print and travel moves roughly followed its contour, it would be ideal to have the nozzle always print normal to the support. However, if the direction to the closest point on the support is used as the normal direction problems occur. When a print path lies close to a vertical wall in the support, the normal direction would be vertical as well, which would result in a crash. Also, the supporting structure might not always be smooth, resulting in a wobbling motion, which is bad for the print.

To overcome these problems, a 'guide surface' was created. This is a smoothly curved surface that follows the contour of the part, but evens out all sharp edges that the support structure has. The guide surface for the SA bracket is shown in Figure 5.9. When generating this surface the clearances of the 5XM that are illustrated in Figure 4.2 are taken into account. Hence the surface incline cannot be too

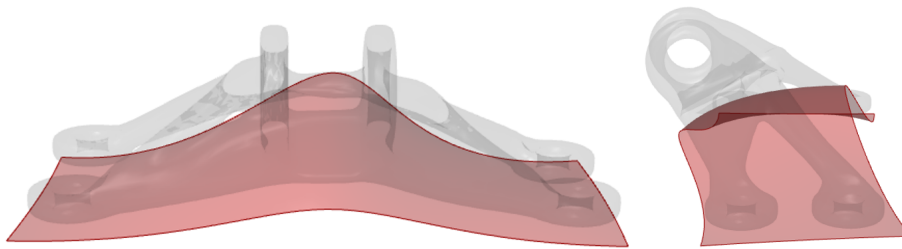


Figure 5.9: Guide surface for the SA bracket. Nozzle will always stay normal to this surface, which will ensure smooth axis movement.

steep, such that the print head never collides with the print bed or support structure. Now, the print head orientation was determined by enforcing that the nozzle is normal to this surface at all times.

5.2.7. G-code generation

In the previous steps, the full print path and the orientation of the head was determined. The next step was to convert this toolpaths into actual G-code. This means the position and orientation of the nozzle tip is converted to X-Y-Z-B-C coordinates. For this process, 5AXISWORKS has developed a grasshopper plugin. The plugin is called 5XMonkey. Essentially, this script converts a single continuous line to G-code using the inverse kinematics of the 5AXISMAKER. This plugin forms the basis of the g-code generation part of this algorithm.

A number of features were changed and added to the plugin to improve its usability. In the basic script, when the C axis rotated more than 360° it would return to 0°. Now that the slip ring was installed, this was not necessary anymore. The slightly altered script keeps an active count on how many full rotations are made and adds the amount times 360 to the C axis angle.

The feed speed calculation was also changed. The set feed speed would only affect the XYZ axis speed. But, it did not take into account the additional movement of the B and C axes, which affects the nozzle tip speed normal to the guide surface. Effectively, it is only controlling the speed of the print head instead of the nozzle tip. This meant that when the distance travelled by the nozzle between two g-code points is larger than the distance travelled by the print head, the nozzle speed was too high. The other way around meant that the nozzle would almost be stationary. This is very bad for print quality since a constant extrusion rate is beneficial. Thus, this was compensated for by multiplying the feed speed by the ratio of print head movement and nozzle tip movement as seen in the equation below.

$$F_{final} = F_{original} * \frac{d_{printhead}}{d_{nozzletip}} \quad (5.1)$$

This was done for each of the G-code points, resulting in each G-code line having its unique feed speed, which ensured a constant nozzle tip speed.

Other changes included a better calculation of the extruder speed, adding an option to specify travel moves where the filament would be retracted, adding a sequence of G-code commands to prime the nozzle before the print and a set of commands to end any print without crashing into the print. Going into detail on these changes would make this report too long and distract from the main results, so it is intentionally left out. The final script is given in Figure 5.10 schematically, where the inputs are coloured yellow and the outputs green.

A couple of the inputs are explained a little more here.

- **Print Line - Curve** - This is the actual line where the material needs to be deposited. It needs to be one continuous line, including all travel moves.
- **Resolution - Integer** - This number specifies the amount of points the curve will be divided into. All the G-code points are spaced evenly, so highly curved print lines need a high resolution to be printed accurately. For this bracket, a spacing of 1 mm is chosen. The lower the resolution, the higher the calculation time.

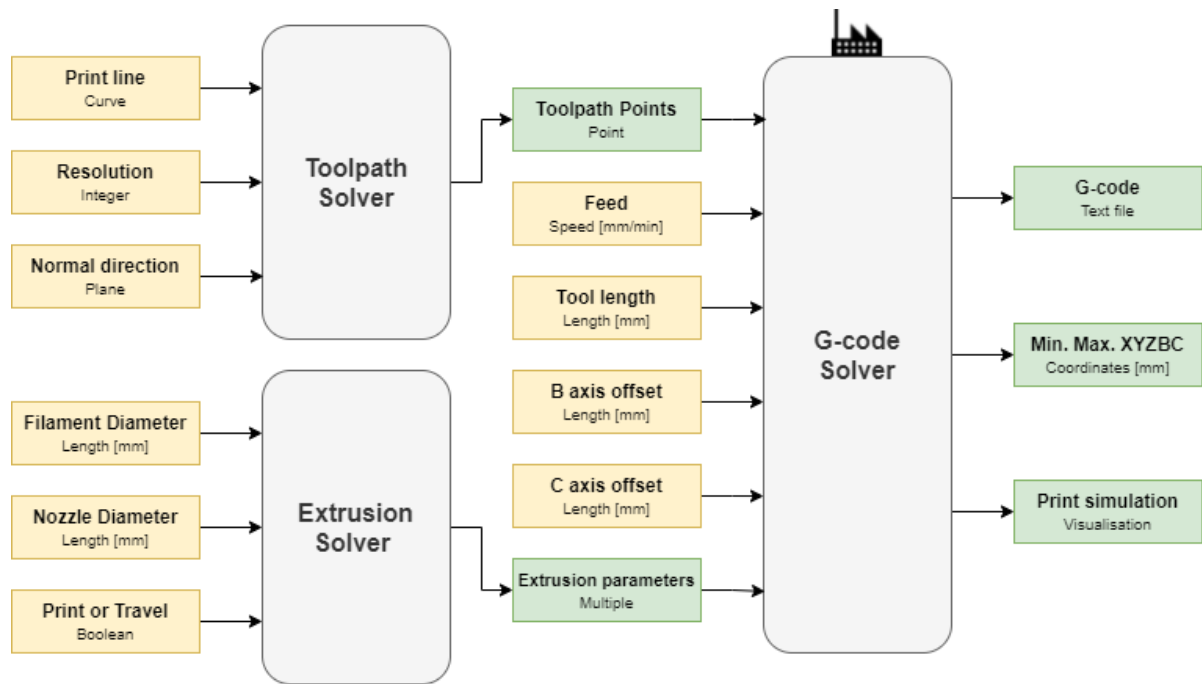


Figure 5.10: Schematic overview of 5XMonkey script

- **Normal Direction - Planes** - These planes determine the normal direction of each G-code point. The number of planes supplied must equal the resolution. If a single plane is supplied, the whole print will be printed in that orientation. If the XY-plane is supplied, it will effectively mimic a 3-axis printer.
- **Print or Travel - Boolean** - This parameter determines whether to extrude or not at each toolpath point. True for print points, and False for travel points. The amount of Booleans needs to equal the resolution.
- **B and C axes offset - Length [mm]** - This incorporates the option to change the print head layout, as was done for this thesis project. The offsets need to be known for the inverse kinematics of the machine. The distances are illustrated in Figure 5.11.

The output of the solver was the full G-code ready to run on Mach3. It also provided the minimum and maximum values of each of the axes, and a visual simulation of the print, ideal for collision checking and debugging before it was run on the printer itself.

5.3. Upper lugs

The third and final part of this bracket were the two lugs that are on top of the part. During the introductory phase of this project, a couple of planar PLA brackets were printed on a conventional 3-axis printer. These were tested under the same load condition as chosen for this project as explained in Section 3.3. It was found that in all of the tests, these two upper lugs were the point of failure. That is why extra attention was spent on printing these upper lugs such that they would be much stronger. Since the thesis aim is to test how much can be gained from SA printing, the upper lugs are effectively over-designed. This way, it is more likely that the stress-optimized main body (part B) will fail during testing, which is the interesting part. In that sense, the upper lugs are only present to enable the test in the first place.

5.3.1. Printing method

When the streamline field from Figure 5.5 is analyzed, it is clear that the upper lugs are not represented. These are points of load introduction, hence the load paths are not well defined. Another method of incorporating these lugs thus had to be found.

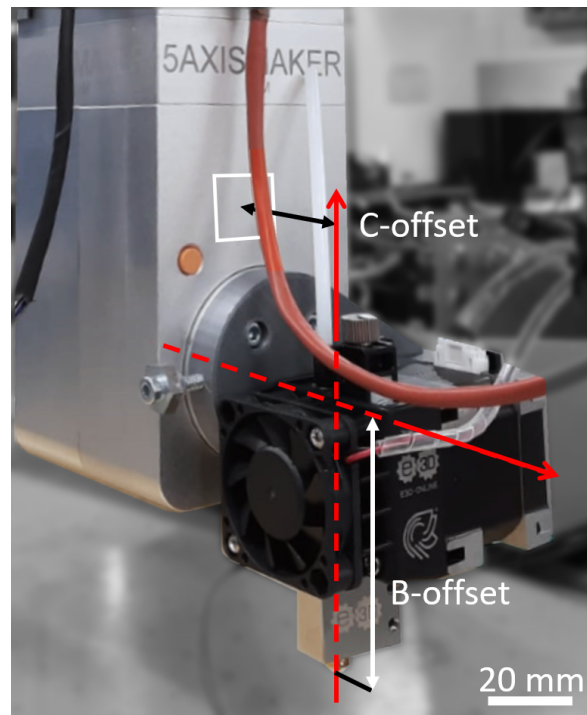


Figure 5.11: B and C axes offset definition

Ideally, the lugs are printed integral to the main body to make the stress lines run continuously. However, this is a very complicated solution since it would require them to be printed in the air, while it would also introduce four extra junctions. As mentioned before, junctions are complicated areas that are prone to being a weak spot. It is deemed a too difficult solution to implement so another method was found.

The streamline field from ParaView did however reveal that the print direction should be concentric with the holes to have maximum strength, and that the stress lines remain in-plane within the lugs. This insight means that the lugs are essentially a planar part, and thus could be printed on a 3-axis printer. During slicing they were oriented such that they lay flat on the print bed. By enforcing the slicer to place the print lines along the outer walls they run concentrically, and therefore are stress-aligned. The layer height was 0.1mm, enhancing the anisotropic behaviour of LCP even more, as shown in Figure 2.8.

5.3.2. Fastening method

A printing method has been described, and now the lugs needed to be fastened to the main body. Again, the focus was on not making the lugs the weak point of the part. The printed lines underneath these upper lugs run horizontally, while the stress lines in the lugs run vertically. Forces must be transferred between these two directions. One option would be to glue/weld the lugs on top of the main body, but this would lead to a weak spot. First of all, if they are welded together, only the top lines of the body would be connected to the lugs. This would not load the bottom lines, which would lead to easy separation in a mode 1 opening force. LCP is bad at withstanding this type of force, since the transverse bonding between the lines is weak.

It was tried to create some sort of mechanical interlocking mechanism between the upper lugs and the body of the part. Inspiration was taken from how rivets fasten two parts together. Rivets use through-hole fastening, with the head on one side being flattened after insertion to interlocks the two parts. 3D Printing is very suitable for this because it offers three advantages over traditional rivets:

1. The rivets can be printed as an integral part of the lug itself. They can be incorporated as pins on the bottom of the lugs, removing the need for a hole in the lug itself.
2. The pins are in the same plane as the lugs themselves. Meaning that with the chosen print

orientation, the printing direction in the pin is along its length. This is exactly the direction the pin will be loaded, making it stress-aligned.

3. Since FFF printers use thermoplastic polymer, the head of the pins need a very small force to be flattened. By applying heat the material softens and deformation becomes easy. It would undo the alignment of the LCP domains in the rivet head, but since the load in the head itself is not aligned with the print direction this is an advantage in this location.

A cross-sectional view of the final fastening is given in Figure 5.12, where the print direction is also clearly illustrated. This design is a very close approximation of the stress lines from the analysis, with both the print lines in the body and the lugs being in the principal stress direction. The fastening method ensures that this transition is not a weak point. To aid correct placement of the lugs onto the main body, both of the lugs were printed together. This also gave space for some extra pins, resulting in a total of 9 pins.

The holes in the body were made using a hot tool to melt through the material. This way no material was removed, but was pressed into the walls of the hole. The walls also got heated, again undoing some of the LCP alignment. This meant the walls of the hole were more solid and exhibit more isotropic behaviour, aiding the load transfer between lug and body.

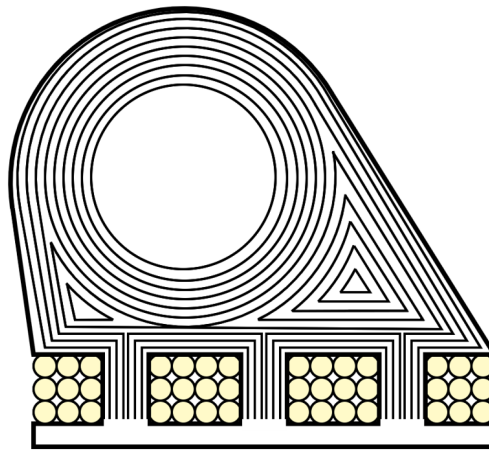


Figure 5.12: Schematic illustration of the print paths in the upper lugs. The paths run concentric around the hole, and along the pins. The bottom part does not show clear lines since it will be thermoformed, and thereby lose its anisotropic behaviour.

6

Results - 3D Printing

In this chapter the physical results of the prints from the 5XM are presented. First, Section 6.1 is devoted to everything regarding the LCP tensile specimens, aimed at investigating LCP properties. In this section, conclusions from the tensile tests will also be drawn. In Section 6.2, the print and test results of the SA bracket are presented. The conclusion and discussion of these tests is left to Chapter 7.

6.1. LCP tensile specimens

To investigate the printing properties of LCP in combination with the new 5-axis printer a set of experiments were performed. A set of tensile specimens were printed and tested on the Zwick test bench presented in Section 4.3. A standard size of 110x5x2 mm was taken. They were printed in different ways which can be found in Table 6.1. This experiment was designed such that the printing temperature, bed temperature, printing speed and orientation could be tested. Where orientation meant if the print would be done laying flat on the heated bed, or against a vertical or diagonal wall as can be seen in Figure 6.1.



Figure 6.1: LCP tensile specimens printed under different orientations. A: Flat on heated bed. B: Vertically against a wall. C: Diagonally against an incline.

During printing, it was found that the interlayer adhesion was worse than expected. When compared to another 3-axis printer the layers delaminated more easily when printed with the same parameters. The suspected cause is a loss in temperature in the nozzle due to its extra length. This meant that the actual temperature the polymer is deposited is lower than the set temperature. Thus, to counter this effect, the nozzle temperature was raised, which reduced the delamination issue.

After the specimens were printed, glass-fiber composite tabs with a bevelled edge were added on the end of each specimen to protect it from damage in the hydraulic grips of the tensile bench. It also provided an some extra surface area to increase the grip. The resulting gauge length was 60 mm. The adhesive was a two-component epoxy by 3M called DP490.

6.1.1. Test results

A summarized version of the results can be seen in Table 6.1. A force-displacement curve of each group of specimens is given in Figure 6.2.

Table 6.1: LCP tensile specimens overview.

Orientation	Nozzle Temp. [°C]	Bed Temp. [°C]	Speed [mm/min]	Specimen Amount	Average E	Average σ_{max} [MPa]
Flat	300	90	1000	3	9.41	164.3 ±27
Flat	300	0	1000	3	8.71	154.2 ±21
Flat	300	90	1500	2	7.28	222.6 ±70
Flat	310	90	1500	4	9.68	221.5 ±46
Vertical	310	0	1500	5	8.65	119.6 ±18
Diagonal	310	0	815	3	10.14	130.5 ±17

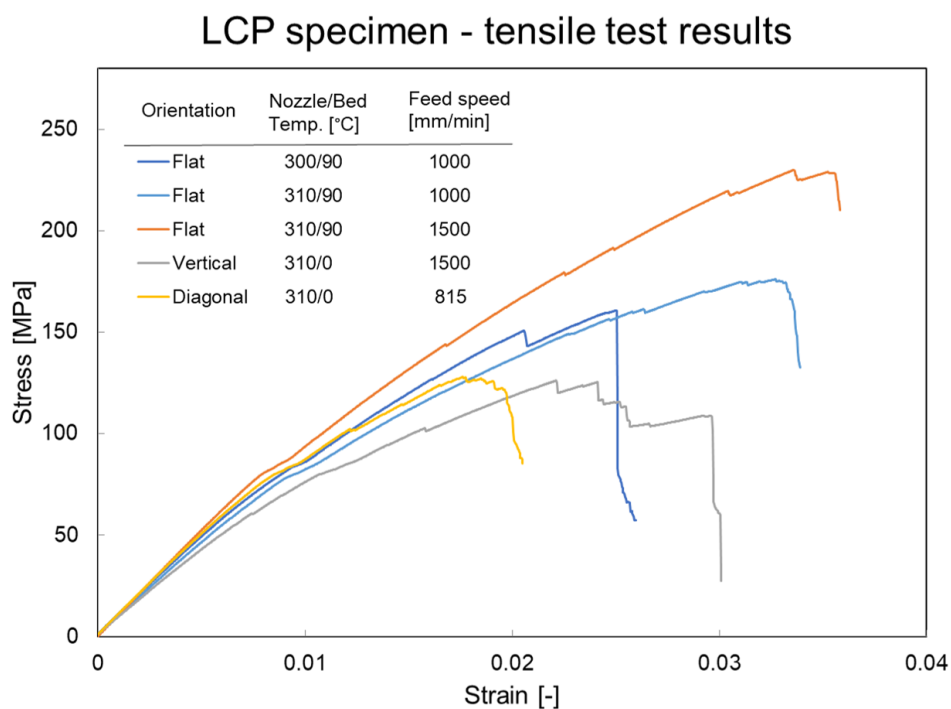


Figure 6.2: Stress strain diagram of a selection of LCP tensile specimens, showing the differences in properties

6.1.2. Conclusion

A couple of conclusions can be drawn from these tests, which can be taken forward in printing the SA bracket.

1. Increasing feed speed seems to have the largest impact on strength. Comparing the flat specimens, the tensile strength was increased by almost 40% on average when the speed was increased from 1000mm/min to 1500mm/min. This is most likely due to the time between two beads of LCP decreasing, thus having less time to cool down and fusing better. Also, quicker nozzle movement puts more shear force on the molten filament possibly increasing the amount of alignment in the nematic domains of the LCP.
2. Printing on top of a heated surface increases the strength. Again, this can be attributed to the improved fusion between two beads when the temperature is higher.

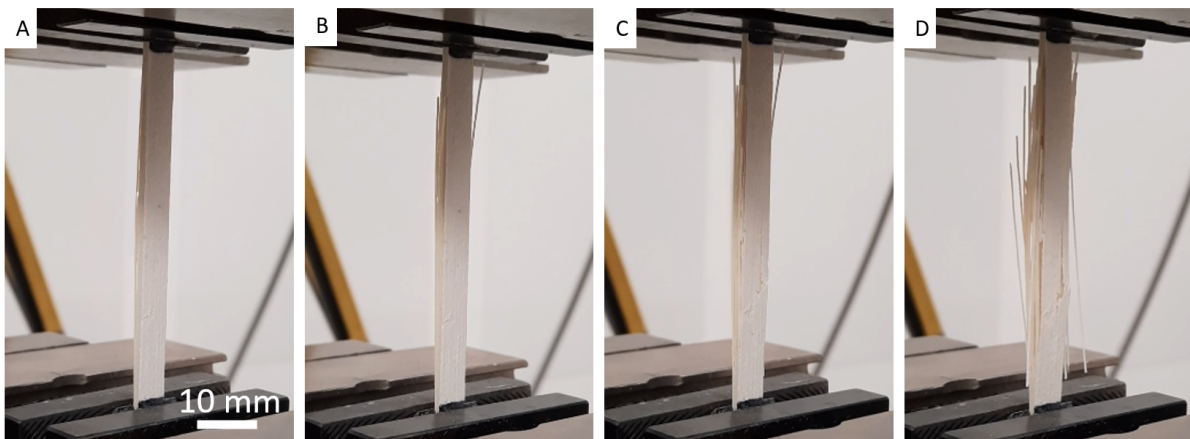


Figure 6.3: LCP tensile test progression. A: Pristine sample. B: First lines started to fail, minor dip in measured force. C: Second failure, the front layer has severed, large dip in measured force. D: Full failure of the specimen determining the ultimate strength.

3. Increasing nozzle temperature enhances the inter-layer adhesion. This was seen during printing, with a couple of lower temperature samples delaminating before the test.
4. The specimens that were not printed flat show a decrease in strength. This can partly be attributed to the fact that they could not be printed on a heated surface.
5. The stress-strain curves show a small s-bend at ± 80 MPa. Since this was present in all specimens at exactly the same force, it was attributed to play in the joints of the tensile test bench. This was confirmed by others that have used this machine.
6. The feed speed when printing diagonally was limited by the maximum speed of the Z-axis.

The failure mode on the strips happened in a cascading fashion. It was audible that some printing lines started to fail before others. This was also visible, as can be seen from the test in Figure 6.3. It can also be seen in the stress-strain diagrams, where a sawtooth behaviour is apparent. This represents lines or layers failing, and other layers being loaded giving the part some residual strength after initial failure. It is also observed that after each failure the stiffness decreases, due to the decrease in cross-section. This decrease in cross-section is not compensated for in the data since this was not measurable. A complete overview of all the test specimens can be found in Appendix C.

6.2. Bracket

Printing the SA bracket was done in a highly iterative manner. Two separate G-codes were developed, one low resolution (meaning very low density) and a high resolution one. The low resolution was used for rapid trials of the printing sequence on the 5-axis printer, while the high-resolution one would be the actual part used for mechanical testing.

Before the print could start, the support structure had to be placed. This needed to be done accurately since misalignment with the print itself would result in a crash. The way this was done was by first printing a 'support guide'. This was the outer contour of the support structure printed on the heated bed. This outer contour could then be used to place the support in. To make sure the support was fixed during the print at all times glue in combination with heat was used. This glue was recommended to use to prevent warping during a print, so it adhered well to the glass-PLA interface. The heated bed was set to 60°C , which was found to be the ideal temperature to aid adhesion, without inducing warping in the support.

The printing temperature of the LCP was chosen to be 330°C . The temperature was raised after the LCP tensile specimens still showed a tendency to delaminate after printing. With this temperature, the strong anisotropic behaviour was reduced, which decreases the strength of the individual lines, but aided the inter-layer bonding which benefited the part as a whole.

The print was started by priming of the nozzle, to ensure the nozzle is full of molten filament before the first line is laid. Then it would run the G-code as explained in Chapter 5. A total of 19 iterations were printed before the end result was deemed to meet the requirements. These iterations mainly involved fixing bugs in the G-code algorithm. The printing process of the final version can be seen in Figure 6.4. A couple of observations were made during the print:

- The line density was very low in the first specimens, so it was slowly increased. This did lead to stronger parts but also lead to more imperfections. It happened when some lines interfered with already printed lines, meaning that the nozzle would travel through already laid-down material. If the density was low enough, the nozzle would comb through the already printed lines, but if it was too high, this led to the nozzle getting stuck and the printer crashing. An optimum in density was found iteratively, with the line density being as high as possible, without leading to a crash.
- Placing the support accurately enough was not possible. There were always a couple of print moves that hit the support. This was not catastrophic since the nozzle was very hot such that it melted the PLA instantaneously. It would however interrupt the printed line, registering it useless in transferring load. This also meant that after one print, the support structure was damaged, making it almost non-reusable.
- The turn-around section printed very well, with good layer adhesion and a smooth surface. The intertwined junction seem to work as intended.
- The travel moves would sometimes also interfere with already printed lines, but it was minimal. When during travel moves extrusion was stopped, the previous line would be pulled off the support. Therefore it was chosen to continue extruding during travel moves. This led to lines in the print not running according to the actual stress direction but it was taken for granted to enable manufacturing.

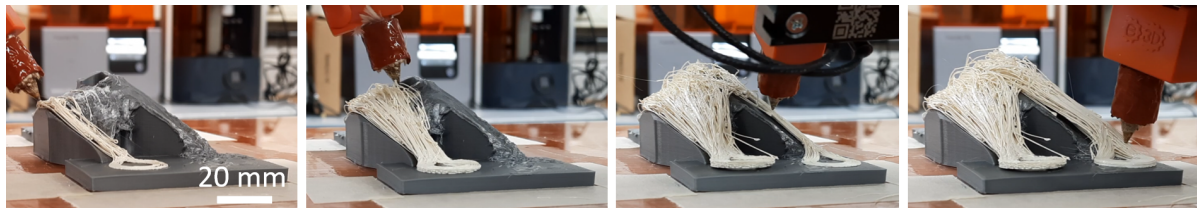


Figure 6.4: Printing process of the main body on the 5XM. A couple of snapshots throughout the print are taken.

Releasing the print from the mould was done mechanically. It did not need a lot of force since by default the bonding between LCP and PLA is weak. Only at places where the nozzle had printed through the supporting structure a cut was needed to separate the part from the support. But since this was already a failed line this did not lead to additional structural changes in the final part.

Printing of the upper lugs was done on a Prusa MK3S which was modified to enable LCP printing. The slicing was done in Ultimaker Cura with the following settings:

- **Nozzle temperature:** 330°C
- **Bed Temperature:** 90°C
- **Print Speed:** 25mm/s
- **Extra features:** Supports, Brim and 100% concentric infill

After the lugs were printed, the supports were removed mechanically. The holes were melted into the main body using a soldering iron. To place the holes correctly a small PLA template was printed and clamped onto the body. After which the lugs were inserted through the nine holes, and a soldering iron was used to flatten out the heads of the pins. The process can be seen in Figure 6.5.

The finished SA bracket can be seen in Figure 6.6



Figure 6.5: Printing and fastening process of the upper lugs. A: Upper lugs as they came out of the printer. B: Pins inserted through nine holes that were made with a soldering iron. C: Pin heads flattened out and integrated with the bracket.

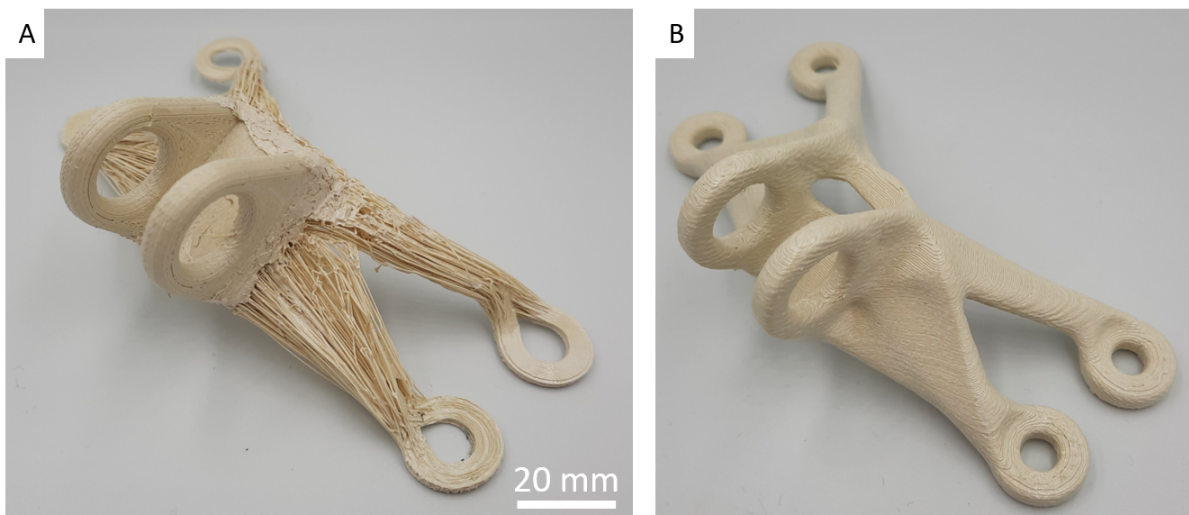


Figure 6.6: Test specimens. A: SA Bracket, B: Planar Bracket

As a baseline test, the bracket was also printed using planar printing on the same printer that was used for the lugs. The same printing settings (temperature and speed) were used as the settings for the SA bracket. This meant that the printing temperature was 330°C, which is not optimal for forming highly anisotropic print lines. But since this print would be loaded transversely to layer direction it was chosen to maintain this high temperature to increase the inter-layer bonding. This bracket can also be seen in Figure 6.6

6.2.1. Test results

Both the SA bracket as the planar bracket were put in the Zwick 20kN tensile test bench. The speed for the test was set to 0.5 mm displacement per minute. The test results are shown in the graph in Figure 6.7.

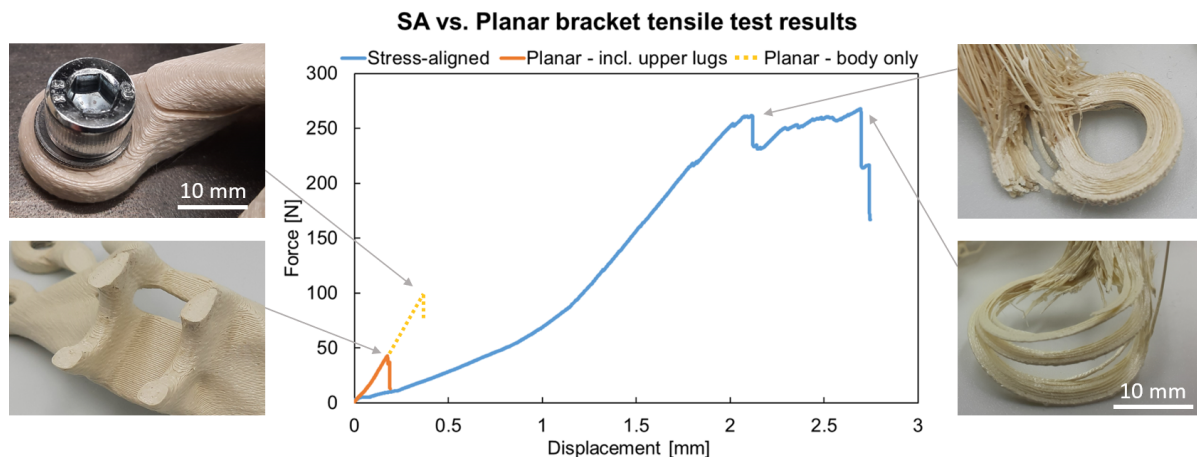


Figure 6.7: Tensile test results of the SA bracket and the planar printed bracket. Pictures of failures included.

The planar bracket failed at 104.6 N, while the SA bracket reached an ultimate force of 269.7 N. This is an increase of 156%. Taking into consideration that weight was also halved from 41.95 g to 20.49 g this is even more striking. Additionally, most of the weight of the SA bracket was situated in the upper lugs since they were solid, which weighed 11.2g. The focus is on the main body, and the lugs are solely there to enable testing, hence the weight of the body alone is more relevant. This means that the planar bracket had a weight of 30.75 g and the stress-aligned one 9.29 g. This meant that the specific strength of the planar bracket was 3.4 N/g and of the SA bracket was 28.8 N/g, thus leading to an improvement of 747%.

The SA bracket showed a failure mode similar to that of the LCP tensile specimens, namely a cascade of failing print lines. This time it was even more severe since the lines acted more as individual lines than as one monolithic structure. The first point of failure was delamination at the front left attachment point, followed shortly by delamination on the rear left attachment point, after which the bracket still had the strength to carry on the test. Nevertheless, it never came close to its first failure point.

The planar bracket was tested twice. In the initial test, the upper lugs delaminated first, at a 50 N tensile force, as expected from the PLA bracket tests. Therefore, to get a better comparison within the main body itself, which is the actual stress-aligned part, it was tested again, by pulling directly on the middle of the main body through a wire. The stiffness of this test is meaningless since the wire was not rigid thus added a lot of extra deformation, the maximum force however is valid, hence why it is represented by a dotted line originating from the first test. This time, the front leg delaminated at 104.6N. The failure modes can also be seen in Figure 6.7.

Stiffness values were also measured. It is clear that the planar bracket is the stiffer one of the two. The SA bracket showed an increase in stiffness during the test, but never really reached the stiffness of the solid LCP bracket. Again as with the tensile specimen test, after initial failure the stiffness decreased drastically.

7

Discussion

In this chapter, the results of the research will be discussed. It starts with conclusions and discussion of the results of the SA bracket in Section 7.1. This is followed up by some remarks of the general application of the SA printing method developed in this research in Section 7.2. The chapter will close with recommendations for future research in Section 7.3.

7.1. Bracket

It is clear that the final strength of the SA bracket leaves something to be desired. Even though a 156% improvement is very impressive, the final strength is not. A set of planar PLA printed brackets were also tested and they reached on average a maximum force of 1230 N (5 brackets). However, PLA exhibits much less anisotropy, meaning that that SA printing PLA will yield less of an improvement than with LCP. In that sense, the higher the anisotropy of a material, the more beneficial it becomes to use SA printing. Besides, the aim of this research was not to compare PLA to LCP, it was to compare planar printing to SA printing which was definitely tested and successfully so. Unfortunately, the full potential of SA printing could not be tested since another weak point led to failure. This will be explained in the following section.

First of all, the failure was at one of the attachment points. This makes sense since the cross-sectional area of the bracket is lowest here, meaning the stress will be the highest. Additionally, the attachment points were (just like the upper lugs) the only location where the printed lines did not lie directly in the stress direction. This means that stress had to travel transverse to the printed direction, causing the delamination. At the junction the print lines also crossed over each other, as can be seen in Figure 7.2. This could have led to printing defects in the form of interrupted lines, explaining the decrease in strength. Taking all of this into account, the lower attachment points were a logical weak point. It also does speak for the SA printing method that the bracket failed exactly where the print was not stress-aligned.

The fact that it failed in a cascading fashion like the LCP test strips was also a sign that not all the lines were loaded equally. Probably one of the lugs was loaded more than the other, or the load case just led to one leg of the bracket being loaded more. It is however a very interesting kind of failure, arguably incorporating a damage-tolerant mechanism. With the first failure not leading to full failure of the part.

A stiffness increase was also observed, which can be explained as follows. During initial loading it was observed that print lines that were not fully along the stress lines were straightened out, leading to high deformation. When more alignment took place, more lines would be loaded and thus the stiffness increased. This is a side effect of a choice that was made in the beginning of the project, namely to only test 1 load case while the bracket was optimized for four load cases. Therefore, the stress lines would not be exactly in the stress direction of this single load case. On one hand this stiffening behaviour is a positive effect, compensating for the misalignment by pulling it in the stress direction, distributing the load more evenly between the individual lines. On the other hand it exposed the bad shear load

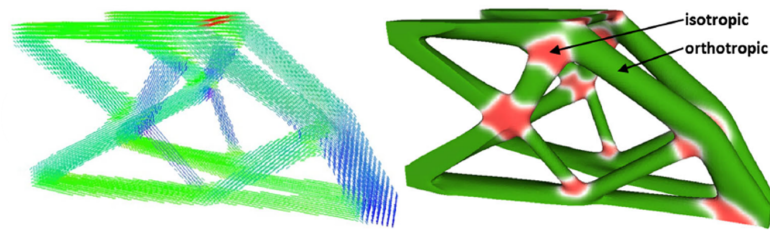


Figure 7.1: Topology optimisation with varying ratio of anisotropy. It is clear that it would be beneficial to have junctions isotropic (red) while the legs should be anisotropic (green). Extracted from Schmidt et al. (2020)

transfer between adjacent lines, due to the low line density. It is comparable to loading a bunch of loose fibres instead of loading a monolithic part with fibres in it.

The density could not be increased because of the way the lines are generated in the first place. The method of randomly seeding the vector field resulted in some of them being very intertwined. This meant that due to the sorting order, crashes would occur if the density would be made any higher. This low density is unfortunately not ideal for LCP because, as shown in Figure 2.8, the strength of LCP increases with decreasing layer height. Lines were oftentimes not printed against any underlying structure, making the line-height the same as the nozzle diameter (0.4mm) which is far from when LCP is at its strongest.

Regarding the travel moves, conclusions can also be drawn. They are conforming to the surface of the part, but the printer does continue extruding during a travel move. This leaves the travel move as a printed line in the part, which can look a bit messy. Some of these travel moves are even perpendicular to the stress lines, which might seem bad for the part. But a case can also be made that continuing extrusion during these travel moves is actually beneficial. During design of composite ply layups, it is said that at least 15% of your plies should lie in each of the principal directions $[0^\circ, 90^\circ, \pm 45^\circ]$ to consolidate it as a single material. The strategy of true SA printing means effectively that all lines lie in the 0° direction, making it not behave as one single material, especially since shear load transfer between the lines was bad. These travel moves connect some of the print lines, essentially acting as the 90° and $\pm 45^\circ$ layers aiding shear load transfer between the lines. Additionally, since lines from two attachment points are printed in an alternating fashion, travel moves would sometimes create stress lines that run left to right continuously.

Sometimes, during a print, the nozzle would interfere with already printed lines. This usually happened where there was a junction. For instance where the front and rear parts of the bracket joined, or where the attachment points were. What happened when the nozzle printed through already printed lines is that it would remelt some of the material around it, fusing it with the current line. However, remelting that area allows the nematic domains in the LCP to reorder back to their random orientation, thereby losing their alignment. This will effectively return that area to isotropic LCP. This is very interesting since it resembles something Schmidt et al. (2020) has found in their optimization algorithm. They ran their algorithm and requested where it would be beneficial to have high anisotropy and where isotropic properties are wanted. Their findings can be seen in Figure 7.1. They found that in junctions, it would be better for the strength of the part to have isotropic properties. Which makes sense, because by definition a junction is a place where the stress is not pointing in one direction but multiple. For this reason, careful remelting at junctions can be used as an opportunity.

Furthermore, the lines at the attachment points are already intertwined quite randomly by the way the stress lines are ordered is discussed in Section 5.2. The resulting intertwined section can be seen in Figure 7.2. The combination of these two effects makes the junction at the attachment points a very good solution. But it was clear from the test that this is still the weak point, due to delamination in the flat area of the turnaround.

7.2. Applicability of stress-aligned printing

It is shown that SA printing has a lot of potential. Although the final product does not excel in its properties, they did increase dramatically compared to planar printing. During the development of this

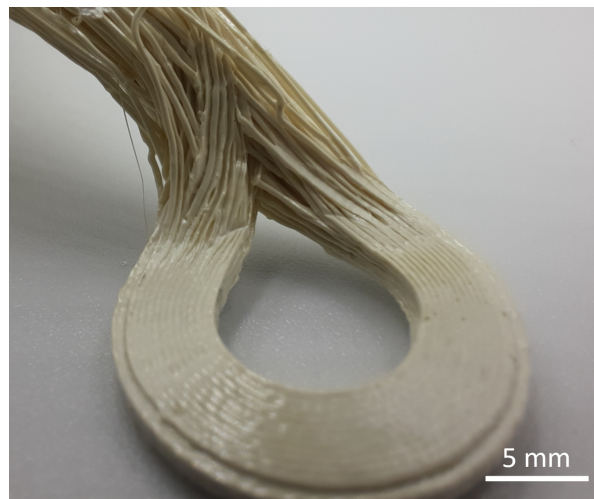


Figure 7.2: Resulting intertwined junction at the attachment point. The randomness in the printing order of the lines makes this junction highly intertwined.

SA bracket, a lot of ideas were worked out and tested which can be used in future prints. For now, they were all tailored to this particular bracket, but they could be developed further to make them more generally applicable.

For instance when looking at the way the normal direction for the print was generated. Using a guide surface to decide the normal direction is very widely applicable. It makes the printer move smoothly, and the guide surface can be made as complex as possible if the support contour needs to be followed more precisely. One small adaptation could be to enforce that the nozzle is also always perpendicular to the print path itself. So instead of finding the closest point on the guide surface in any direction, it could only search for the closest point in the plane perpendicular to the print path. This way the nozzle is always oriented 90 degrees relative to the print direction, resulting in optimal forces on the flow of molten filament.

The method for printing along stress direction could also be applied in any type of part. Even for much simpler parts. One does not need a topology optimized part where the fibre directions are already laid out. With any part and load case, a Finite Element Analysis (FEA) can be done from which the stress lines could be extracted. This can be used as guides for many prints, even on a 3-axis printer.

SA printing is only tested on LCP in this research, but it can also be tested using other 3D printing filament. As mentioned before, the higher the anisotropy, the higher the incentive to use SA printing. For instance the CFRP filaments which were discussed in the literature review (Section 2.2). These would also be very suitable for 5-axis SA printing. This would be the ultimate form of carbon fibre steering. However the downside of these materials is their limit in bending radius, since the carbon fibre itself remains very stiff when depositing. This is a problem that LCP does not have. The algorithm by Schmidt et al. (2020) does account for this though, where a minimum bending radius can be specified, for which it will optimize the part.

7.3. Future research recommendations

Most of the recommendations for improving this stress-aligned print are centered around the idea of increasing the density of the print. This is limited by the current algorithm, however an increase in line density will enable more interline adhesion thus better load transfer between lines, making the material act more monolithic. This will most definitely improve the mechanical properties.

The most simple way to achieve this without changing the current print a lot is by transforming it into a composite structure. The printed lines could be seen as the fibres of a material, which will have to be cast in a resin. This mimics the way carbon fibre reinforced plastics are made, but then with LCP fibres. LCP has been shown to reach properties as strong as carbon fibre, and does not have a limited steering radius. A mould could be made to pour epoxy resin in, which will fill the outer contour of the part. As an added benefit, this will also probably solve the delamination in the attachment points from

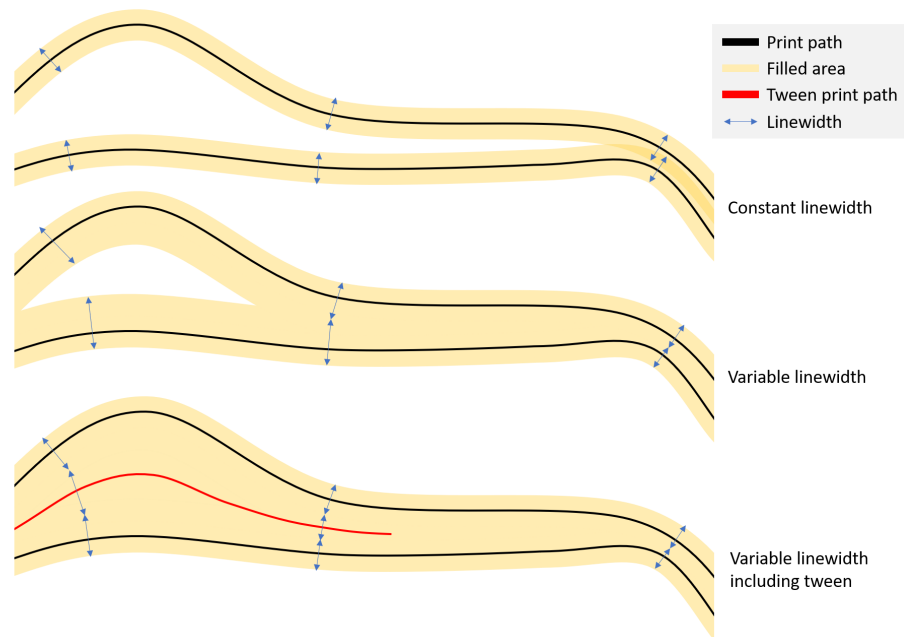


Figure 7.3: 2D representation of how variable extrusion rate and adding tween lines can increase the density of a print.

the tensile tests, and provide another solution to attach the upper lugs without using the pins. And finally, a point can also be made about the improved aesthetics of making the bracket this way.

This resin however increases the amount of manufacturing steps needed. Additionally, if the density of the printed lines is very low, the fibre volume fraction of the part will become very low. One can then argue that the mechanical properties are more determined by the resin than by the fibres. It would thus be much better if no resin is needed to increase the density. The strength of LCP lies in the fact that it is a fibre reinforced material by itself. It also saves a lot of time if it can be done in only one manufacturing step.

A method for achieving higher density without the use of a resin is to alter the extrusion rate at certain points. Where the density is very low, a higher extrusion rate could be applied. Ideally, the extrusion rate is calculated such that it fills a certain cross-section. This could be achieved by calculating the distance to the nearest line or nearest set of lines at a certain cross-section, and ensuring that the line fills the space between those lines. At certain locations, the line density is so low that the extrusion rate has to become unrealistically large, to the point where extruding so much material does not form a neat line anymore. In that case, another method to try could be to add extra lines which are so-called 'twens' of the current stress lines. A tween is a line that always lies exactly in the middle of two adjacent lines. This way, extra lines are added which also follow the stress direction since they follow the adjacent lines. The potential gain in density is illustrated in a 2D representation in Figure 7.3 but can be just as applicable to 3D cases.

An increase in density could also be achieved by changing the seed method for the integration of the vector field. Currently, the vector field is seeded randomly, which lead to a quite even distribution of stress lines, but they do not form layers. This makes the sorting of the lines such that there is no interference with other printed lines almost impossible. A better way of generating the stress lines might be to seed by an ordered grid of points. This could create lines that are less intertwined making them easier to sort and not interfere with each other so much. Thus the line density can most definitely increase in this case. However, this method would approach the print becoming a curved-layer print like the one in Fang et al. (2020). These individual layers still suffer from weak bonding, and delaminations can happen earlier. An optimum thus has to be found between the severity of the intertwined lines, and the line density that it allows. Too many intertwined lines and the density needs to be very low to not crash during the print, but too few intertwined lines make it more prone to delamination. To try this, another tool has to be found/developed to perform the Runge-Kutta integration of the vector field, since the Streamtracer from ParaView is quite limited in choosing how to place the seeds.

Another benefit of the curved-layer approach mentioned above is that the chance of having an underlying surface to print on is increased. This way the print line-height can be tuned better. By printing at a small layer height one effectively prints a wide tape of LCP, which are much stronger. It is however always in balance with the inter-layer adhesion, with higher anisotropy meaning lower inter-layer adhesion. So an optimum could be found here. Another way of trying to improve the strength by having higher anisotropy would be to try to print this with a smaller nozzle size. This way if a line is printed in mid-air, as it would sometimes be on this print, the diameter is still small meaning the shell-to-core ratio of the LCP bead would be high.

A potential improvement that is not really focused on obtaining higher density is to look at the travel moves. It might be beneficial to try to optimize retraction such that no string is left behind when the filament is retracted. This would enable to stop the extrusion during travel moves and only the pure stress lines are printed. What would help in this case is to sort the stress lines such that the travel move never reverses the print direction, to aid shearing off the nozzle from the printed line. Another improvement to the travel moves would be to find an optimum between the higher and lower options as shown in Figure 7.4. Here, to prevent the horizontal or vertical move, a line in the middle has to be found. This could be achieved through interpolating between the two travel paths, as to slowly transition from the height of one point to the other height. If this is implemented the travel moves are fully continuous without erratic vertical and horizontal pieces.

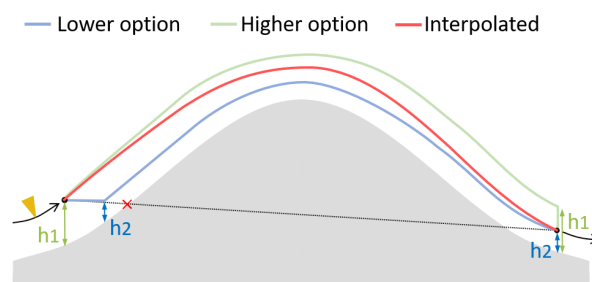
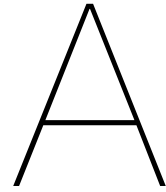


Figure 7.4: Possible improved travel move, smoothly transitioning between the lower and higher options.

A final improvement to the travel moves would be to implement a method to stress-align them as well. In the current algorithm, this is just a straight path in the X and Y direction, and following the support contour in the Z-direction. To make the travel moves indistinguishable from the stress lines, the original vector field can be used as a guide. An algorithm could be developed which finds a line between two points following the vector field as closely as possible. It will never be perfectly stress-aligned since the two points between which is travelled do not lie in a single stress line, but it could be approximated better in this way. This results in added strength since the travel moves also carry the load more effectively.

Finally, to improve the current SA bracket is is good to see if it can be printed as a single print. Integrating the upper lugs in the print would circumvent the need for fastening. Additionally, it will save production time and manual labour. For inserting the pins holes have to melted into the part which interrupts the stress lines. Ideally these stress lines will smoothly transition into the upper lugs as well. A similar approach to how the lower attachment points were done can be taken. LCP is very stiff when it exits the nozzle, hence printing in mid-air might be an option to investigate. Or a clever way of including some sort of support should be found. This does however add extra junctions in the print which potentially lead to a weak point. And one has to make sure that those junctions are also intertwined with the lines passing through the main body. Since if the lugs are simply printed on top of the main body this will create a weak weld line where it would delaminate easily when loaded.

On a completely different note, it might be worthwhile to start research on how to print strong junctions in 5-axis printing in general. This is an essential element for the feasibility of SA printing, or printing strong parts in general. In this research project, it was found numerous times how weak such points can be compared to the rest of the print. Eventually, the result was also decided by a junction where the load was introduced, which turned out to be the weak point. Here, one could take inspiration from nature. The behaviour of a tree grains could be matched more closely, with real spiral print paths which are mechanically interlocked. Or potentially trying to mimic is how trees incorporate branches in their grains to make them very strong. But other methods could also be developed and tested. It would benefit the nonplanar and planar FFF research as a whole when strong junctions can be printed using continuous print paths.



Wiring diagrams 5-axis printer setup

The first table presents the wiring of the slip ring, in the second figure the pin-outs for the four connectors to and from the slip ring is given. The last diagram shows the internal structure of the heated bed control box.

Component	Subcomponent	Print Head Side			Slipping			Frame side	
		Wire	Color	Current	Wire	Color	Amps	Color	Cable nr: Component
Hemera Extruder Unit	Thermistor PT100	Signal	Red	variable	1- Red	Yellow	Low	White	Inkbird PID
		Ground	Red	variable	1- Red	Light Green	Low	Yellow	Inkbird PID
	Heating cartridge	Input	Green	3.33A	1- Red	Brown/Orange	High	Green	Inkbird PID
		Ground	Green	3.33A	1- Red	Black/Grey	High	Brown	Inkbird PID
	Heatsink Fan	12V	Red	0.08A	1- Red	Purple	Low	Green	9 PSU
		Ground	Black	0.08A	1- Red	White	Low	White	9 PSU
	Extruder stepper motor	A+	Blue	1.33A	1- Red	Dark Blue	Low	Red	1 PSU
		A-	Red	1.33A	1- Red	Light Blue	Low	Blue	1 PSU
		B+	Green	1.33A	1- Red	Light Brown	Low	Green	1 PSU
		B-	Black	1.33A	1- Red	Red	Low	Black	1 PSU
B-C axis motors	B-Axis Stepper	A+	Red	1.33A	2- Black	Orange	Low	Red	PSU
		A-	Blue	1.33A	2- Black	Grey	Low	Blue	PSU
		B+	Green	1.33A	2- Black	Yellow	Low	Green	2 PSU
		B-	Black	1.33A	2- Black	Red	Low	Black	PSU
	C-Axis Stepper	A+	Red	1.33A	2- Black	Purple	Low	Red	PSU
		A-	Blue	1.33A	2- Black	Dark Blue	Low	Blue	3 PSU
		B+	Green	1.33A	2- Black	Black	Low	Green	PSU
		B-	Black	1.33A	2- Black	White	Low	Black	PSU
		Signal	Black	low	2- Black	Light Brown	Low	Black	PSU
		Ground	Blue	low	2- Black	Light Green	Low	Blue	10 PSU
Sensors	BC Sensor	12V power	Brown	low	2- Black	Light Blue	Low	Brown	PSU
		Ground	Blue	low	2- Black	Light Green	Low	Blue	PSU

Figure A.1: Wiring table of the slipping

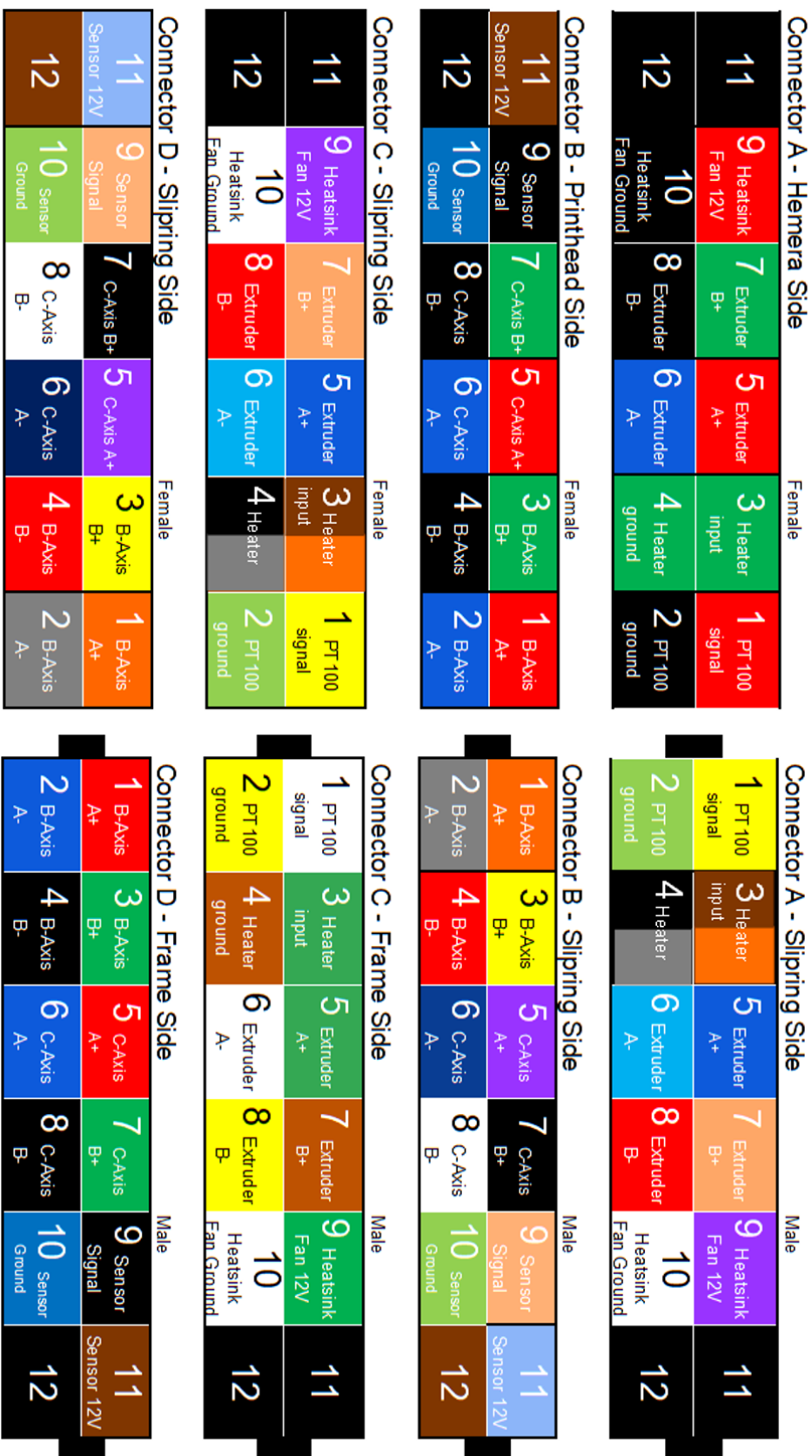


Figure A.2: Pinouts of the connectors before and after the slip ring

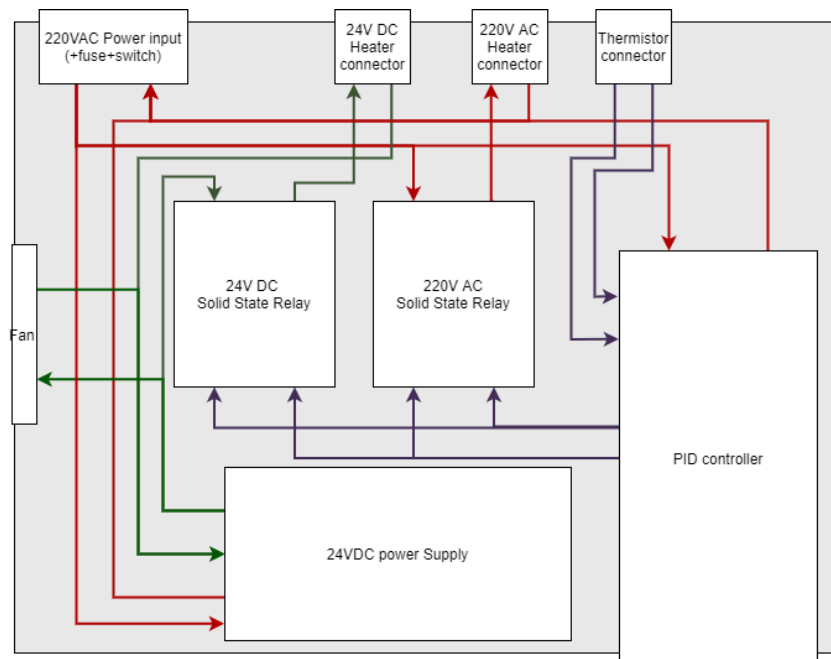
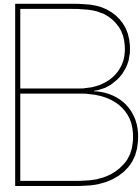


Figure A.3: Internal wiring diagram of heated bed control box. Which both supports temperature control of a 360 V AC and 24V DC heating device.



Stream tracer parameters

The parameters used in the stream tracer in ParaView for generating the streamlines from the vector field are shown here.

Properties (StreamTracer1)

Vectors ▼
vectorField

Interpolator Type ▼
Interpolator with Point Locator

Surface Streamlines

Integration Parameters

Integration Direction ▼
BOTH

Integrator Type ▼
Runge-Kutta 4-5

Integration Step Unit ▼
Cell Length

Initial Step Length ▢
0.2

Minimum Step Length ▢
0.01

Maximum Step Length ▢
0.5

Maximum Error ▢
1e-06

Streamline Parameters

Maximum Steps ▢
2000

Maximum Streamline Length ▢

 184.354
 ✕
↺

Terminal Speed ▢
0.5

Compute Vorticity

Seeds

Seed Type ▼
Point Cloud

Point Cloud Parameters

Show Sphere

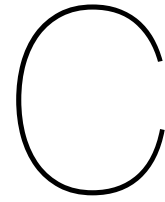
Center ▢

Radius ▢

Note: Use 'P' to a 'Center' on mesh or 'Ctrl+P' to snap to the closest mesh point

Number Of Points ▢
31000

Figure B.1: Parameters used for the stream tracer in ParaView



LCP tensile specimens test results

Table C.1: Overview of all tensile specimen

Spec. Number	Print Orientation	Nozzle T. °C	Bed T. °C	Speed mm/min	thickness mm	width mm	length mm	Fmax N
1	Flat	300	90	1000	1.96	5.51	59.8	1452
2	Flat	300	90	1000	1.91	5.25	59.8	1890
3	Flat	300	90	1000	1.95	5.46	60.6	1711
4	Flat	300	0	1000	2.05	5.33	59.8	1490
5	Flat	300	0	1000	2.05	5.25	60.25	1894
6	Flat	300	0	1000	2.04	5.15	60	1578
7	Flat	300	90	1500	1.88	5.3	60.58	2931
8	Flat	300	90	1500	1.87	5.3	60.25	1496
9	Flat	310	0	1500	1.98	5.1	60.1	1692
10	Flat	310	0	1500	1.99	5.2	60.7	989
11	Flat	310	90	1500	1.91	5.2	60.3	2583
12	Flat	310	90	1500	1.9	5.2	6.25	2341
13	Vertical	310	0	1500	2.12	5.33	60.8	1348
14	Vertical	310	0	1500	1.94	5.37	60.1	1155
15	Vertical	310	0	1500	2.04	5.43	60.2	1351
16	Vertical	310	0	1500	2	5.36	60.6	1351
17	Vertical	310	0	1500	1.65	5.25	60.5	1235
18	Diagonal	310	0	815	2.03	5.48	60.8	1711
19	Diagonal	310	0	815	2.08	5.29	59.7	1404
20	Diagonal	310	0	815	2.06	5.28	60.9	1391

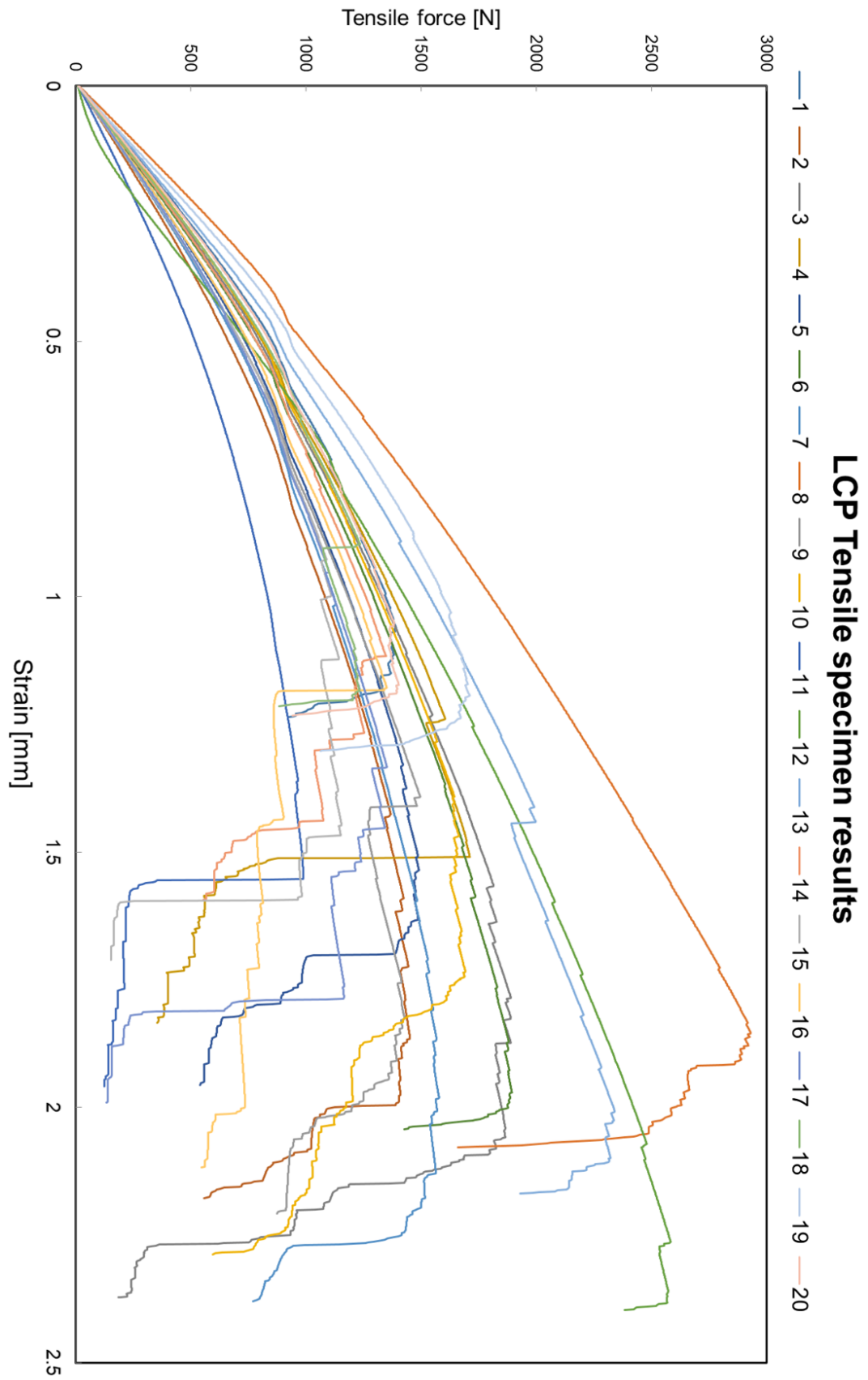


Figure C.1: Tensile tests of all the LCP test specimen

Bibliography

- 5AXISWORKS LTD (2020). *5AXISMAKER*. URL: <https://www.5axismaker.com/> (visited on 01/21/2021).
- Ahn, Sung Hoon, Michael Montero, Dan Odell, Shad Roundy, and Paul K. Wright (2002). "Anisotropic material properties of fused deposition modeling ABS". In: *Rapid Prototyping Journal* 8.4, pp. 248–257. ISSN: 1355-2546. DOI: 10.1108/13552540210441166.
- Crump, Scott (June 9, 1992). "Apparatus and Method For Creating Three-Dimensional Objects". U.S. pat. 5121329. Stratasys, Inc.
- Dai, Chengkai, Charlie C. L. Wang, Chenming Wu, Sylvain Lefebvre, Guoxin Fang, and Yong-Jin Liu (2018). "Support-free volume printing by multi-axis motion". In: *ACM Transactions on Graphics* 37.4, pp. 1–14. ISSN: 0730-0301. DOI: 10.1145/3197517.3201342.
- Ding, Donghong, Zengxi Pan, Dominic Cuiuri, Huijun Li, Nathan Larkin, and Stephen Van Duin (2016). "Automatic multi-direction slicing algorithms for wire based additive manufacturing". In: *Robotics and Computer-Integrated Manufacturing* 37, pp. 139–150. ISSN: 0736-5845. DOI: 10.1016/j.rcim.2015.09.002.
- Etienne, Jimmy, Nicolas Ray, Daniele Panozzo, Samuel Hornus, Charlie C. L. Wang, Jonàs Martínez, Sara McMains, Marc Alexa, Brian Wyvill, and Sylvain Lefebvre (2019). "CurviSlicer: Slightly curved slicing for 3-axis printers". In: *ACM Transactions on Graphics* 38.4, pp. 1–11. ISSN: 0730-0301 1557-7368. DOI: 10.1145/3306346.3323022.
- Faber, Nick (2020). "Non-planar Fused Deposition Modeling; a Literature Review". Literature Review. Delft Technical University.
- Fang, Guoxin, Tianyu Zhang, Sikai Zhong, Xiangjia Chen, Zichun Zhong, and Charlie C.L. Wang (2020). "Reinforced FDM: Multi-Axis Filament Alignment with Controlled Anisotropic Strength". In: *ACM Transactions on Graphics* 39.6. DOI: 10.1145/3414685.3417834.
- Gantenbein, Silvan, Kunal Masania, Wilhelm Woigk, Jens P. W. Sesseg, Theo A. Tervoort, and André R. Studart (2018). "Three-dimensional printing of hierarchical liquid-crystal-polymer structures". In: *Nature* 561.7722, pp. 226–230. ISSN: 0028-0836. DOI: 10.1038/s41586-018-0474-7.
- Gibson, Ian, David Rosen, and Brent Stucker (2010). *Additive Manufacturing Technologies; 3D Printing, Rapid Prototyping, and Direct Digital Manufacturing*. 2nd Edition. Springer.
- GrabCAD (2013). *GE Jet Engine Bracket Challenge*. URL: <https://grabcad.com/challenges/ge-jet-engine-bracket-challenge>.
- Houriet, Caroline (2019). "Manufacturing of Liquid Crystal Polymers Interlayer features: formation & impact on interlaminar shear strength". Master's Thesis. Delft Technical University.
- Huang, Yijiang, Josephine Carstensen, Lavender Tessmer, and Caitlin Mueller (2019). "Robotic Extrusion of Architectural Structures with Nonstandard Topology". In: *Robotic Fabrication in Architecture, Art and Design*, pp. 377–389. DOI: 10.1007/978-3-319-92294-2_29.
- Khurana, J. B., T. W. Simpson, and M. Frecker (2018). "Structurally intelligent 3D layer generation for active-Z printing". In: International Solid Freeform Fabrication Symposium 2018 - SFF'18. Austin TX, USA, pp. 2413–2426.
- Kitware (2020). *Paraview*. URL: <https://www.paraview.org/> (visited on 10/25/2021).
- Kubalak, Joseph R., Alfred L. Wicks, and Christopher B. Williams (2019). "Exploring multi-axis material extrusion additive manufacturing for improving mechanical properties of printed parts". In: *Rapid Prototyping Journal* 25.2, pp. 356–362. ISSN: 1355-2546. DOI: 10.1108/rpj-02-2018-0035.
- Matsuzaki, Ryosuke, Taishi Nakamura, Kentaro Sugiyama, Masahito Ueda, Akira Todoroki, Yoshiyasu Hirano, and Yusuke Yamagata (2018). "Effects of Set Curvature and Fiber Bundle Size on the Printed Radius of Curvature by a Continuous Carbon Fiber Composite 3D Printer". In: *Additive Manufacturing* 24, pp. 93–102. ISSN: 2214-8604. DOI: 10.1016/j.addma.2018.09.019.
- Matsuzaki, Ryosuke, Masahito Ueda, Masaki Namiki, Tae-Kun Jeong, Hirotsuke Asahara, Keisuke Horiguchi, Taishi Nakamura, Akira Todoroki, and Yoshiyasu Hirano (2016). "Three-dimensional printing of continuous-fiber composites by in-nozzle impregnation". In: *Scientific Reports* 6.1, p. 23058. ISSN: 2045-2322. DOI: 10.1038/srep23058.

- Mueller, Stefanie, Sangha Im, Serafima Gurevich, Alexander Teibrich, Lisa Pfisterer, François Guimbretière, and Patrick Baudisch (2014). "WirePrint: 3D Printed Previews for Fast Prototyping". In: ACM symposium on User interface software and technology - UIST '14. Honolulu Hawaii, USA. DOI: 10.1145/2642918.2647359.
- Ranelucci, A. (2011). *Slic3r*. Version 1.3.0. URL: <https://slic3r.org/>.
- Robert McNeel and Associates (1993). *Rhinoceros*. Version 6. URL: <https://www.rhino3d.com/> (visited on 12/18/2020).
- Schmidt, Martin-Pierre, Laura Couret, Christian Gout, and Claus B. W. Pedersen (2020). "Structural topology optimization with smoothly varying fiber orientations". In: *Structural and Multidisciplinary Optimization* 62.6, pp. 3105–3126. ISSN: 1615-147X 1615-1488. DOI: 10.1007/s00158-020-02657-6.
- Singamneni, Sarat, Asimava Roychoudhury, Olaf Diegel, and Bin Huang (2012). "Modeling and evaluation of curved layer fused deposition". In: *Journal of Materials Processing Technology* 212.1, pp. 27–35. ISSN: 0924-0136. DOI: 10.1016/j.jmatprotec.2011.08.001.
- Slater, Duncan, Robert S. Bradley, Philip J. Withers, and A. Roland Ennos (2014). "The anatomy and grain pattern in forks of hazel (*Corylus avellana* L.) and other tree species". In: *Trees* 28.5, pp. 1437–1448. ISSN: 0931-1890 1432-2285. DOI: 10.1007/s00468-014-1047-5.
- Turner, Brian N., Robert Strong, and Scott A. Gold (2014). "A review of melt extrusion additive manufacturing processes: I. Process design and modeling". In: *Rapid Prototyping Journal* 20.3, pp. 192–204. ISSN: 1355-2546. DOI: 10.1108/rpj-01-2013-0012.
- Ultimaker (2020). *Cura*. Version 4.8. URL: <https://ultimaker.com/nl/software/ultimaker-cura> (visited on 01/10/2021).
- Wang, Mingqian, Haiguang Zhang, Qingxi Hu, Di Liu, and Herfried Lammer (2019). "Research and implementation of a non-supporting 3D printing method based on 5-axis dynamic slice algorithm". In: *Robotics and Computer-Integrated Manufacturing* 57, pp. 496–505. ISSN: 0736-5845. DOI: 10.1016/j.rcim.2019.01.007.
- Wu, Chenming, Chengkai Dai, Guoxin Fang, Yong-Jin Liu, and Charlie C. L. Wang (2020). "General Support-Effective Decomposition for Multi-Directional 3-D Printing". In: *IEEE Transactions on Automation Science and Engineering* 17.2, pp. 599–610. ISSN: 1545-5955. DOI: 10.1109/tase.2019.2938219.
- Xiao, Xinyi and Sanjay Joshi (2020). "Process planning for five-axis support free additive manufacturing". In: *Additive Manufacturing* 36, p. 101569. ISSN: 2214-8604. DOI: 10.1016/j.addma.2020.101569.
- Xu, Ke, Lufeng Chen, and Kai Tang (2019). "Support-Free Layered Process Planning Toward 3 + 2-Axis Additive Manufacturing". In: *IEEE Transactions on Automation Science and Engineering* 16.2, pp. 838–850. ISSN: 1545-5955 1558-3783. DOI: 10.1109/tase.2018.2867230.
- Yerazunis, W.S., J.C. Barnwell III, and D.N. Nikovski (2016). "Strengthening ABS, Nylon, and Polyester 3D Printed Parts by Stress Tensor Aligned Deposition Paths and Five-Axis Printing". In: International Solid Freeform Fabrication Symposium 2016, SSF '16. Austin TX, USA.